Ball vibration absorbers with radially-increasing rolling friction

Ball vibration absorbers with radially-increasing rolling friction

Emiliano Matta

Politecnico di Torino, Department of Architecture and Design, Viale Mattioli 39, Turin, Italy
E-mail: emiliano.matta@polito.it · Phone: +39 011 090 4867 · ORCID: 0000-0001-5453-1470

Abstract
Ball vibration absorbers (BAs) are a simple, low-cost and compact way to realize the principle of tuned mass damping. The basic arrangement of a BA consists of a spherical mass rolling without sliding in a rubber-coated spherical cavity, and dissipating through rolling friction. In a conventional BA, the rubber coating is uniform along the cavity, and so is rolling friction. This makes the BA equivalent damping inversely proportional to the excitation amplitude, and its performance amplitude dependent. In this study, two new BA types are proposed. The first type, called the homogeneous BA (HBA), has a rolling friction radially increasing in proportion to the ball angular displacement. Hardly realizable in practice, this ideal friction model is homogeneous in the first order, ensuring an amplitude-independent optimal performance. The second type, called the discrete-homogeneous BA (DBA), is the stepwise approximation of the HBA. Not exactly homogeneous, its variable friction model can be easily realized through the juxtaposition of multiple coating regions, having different thickness or material quality. After establishing a unifying, fully nonlinear, nonholonomic analytical model, valid for various types of friction and viscous BAs, this paper first derives an optimal design procedure applicable to each type, then experimentally and numerically demonstrates (1) the validity of the homogeneous and discrete-homogeneous concepts, (2) their practical feasibility, (3) the accuracy of the proposed model, (4) the effectiveness of the design procedure, and (5) the superior performance of the HBA and the DBA over conventional friction absorbers.

Keywords: passive structural control; ball vibration absorber; nonholonomic dynamics; rolling resistance; spatially variable friction; discretized homogeneous damping; optimal design; experimental validation.

1 Introduction

Dynamic vibration absorbers (DVAs), also known as tuned mass dampers (TMDs), are widespread passive control devices, extensively studied and applied on flexible, low-damped structures, to reduce their resonance response under various external dynamic disturbances, including wind, seismic, hydrodynamic, industrial, transport and other loads [1-13]. Conceived as single-degree-of-freedom (SDOF) linear appendages of the main structure, they absorb and dissipate vibrational energy from a selected (target) structural mode, if optimally tuned to its frequency and appropriately damped.

Depending if their restoring force is elastic or gravitational, DVAs are categorized in spring and pendulum types, and pendulum types are further classified in hanging pendulums and supported pendulums, depending if their mass is suspended through ropes or bars, or constrained to move on a physical concavity. Supported pendulums, compact and geometrically versatile, are increasingly popular, and can be realized in a variety of configurations, including rolling, sliding, and rocking pendulums [14, 15], unbalanced pendulums [16], track nonlinear energy sinks (NESs) [17], and ball pendulums [18] (Figure 1). Each configuration can be arranged as a unidirectional or a bidirectional system, in this latter case using either a pair of mutually orthogonal rails mounted in series, or one spatial pendulum surface, ideally non-axial-symmetrical if the two principal structural frequencies are different [19].

Among supported pendulum DVAs, the ball pendulum absorber (BA) (Figure 1f) is a simple, low-cost, compact and easy maintenance device, especially recommended on structures where a limited vertical and horizontal space is available for an absorber installation, such as TV towers, wind turbine towers, masts, antennas, and bridges [20]. Invented in the early ‘90s by Pirner, originally in the form of an oblong container with a heavy ball inside, aimed to reduce the transversal vibrations of a suspended footbridge [21], it is later installed by the same author on two TV towers, “as there was not enough space at the top of the tower for an absorber of the standard pendulum type” [18]. This time, it is in the form later become

typical of BAs: a rubber-coated steel dish shaped as a spherical cap, inside which a steel sphere of a smaller radius rolls without sliding. The difference of the two radii determines the rolling frequency, while the quality of the contact surfaces determines the energy dissipation properties. The device, enclosed in an airtight case, is virtually maintenance free. Its equivalent damping ratio is nearly inversely proportional to the ball motion amplitude, as shown through forced vibration tests on real scale prototypes [18, 20]. After Pirner, the BA concept is theoretically investigated by various authors [22-24], and recently applied to the vibration control of wind turbine towers and building structures. For example, in [25] a BA is proposed for installation in the nacelle of a wind turbine tower, after excluding a standard pendulum absorber because of space limitations. A 1/20-scale model of the tower-BA combined system is shaking-table tested, the BA consisting of single or multiple steel balls, rolling inside an uncoated plastic spherical container and dissipating through rolling friction and mutual impact. In [26], a BA is chosen for controlling an offshore wind turbine tower, preferred over a spring TMD because more compact and easier to maintain. Its effectiveness is proven through shaking-table tests on a 1/13-scale tower-BA model, the BA being in this case a unidirectional device, made of a steel ball rolling inside a cylindrical rubber-coated container. In [27], several BAs are supposed to be distributed in the hollow floors of a building structure, to reduce its seismic response. Each BA consists of a steel ball, embedded in a plastic hollow module of a biaxial voided slab, and rolling on its bottom surface, shaped as a spherical cap. The solution is simple and unobtrusive, and its efficacy is demonstrated numerically. In these examples [25-27], simulations are run using unidirectional dynamic models obtained through Lagrange's equations, with the BA dissipation mechanism represented as a dry rolling friction.

To the author's knowledge, a common feature to existing BAs is the adoption of a uniform rolling surface, which can be that of the container itself or more often that of an adhered elastomeric layer. This is also the case for all known types of rolling ball isolation devices, i.e. base isolation systems consisting of single or multiple balls rolling between counter-facing surfaces (typically spherical, conical, or flat), for the seismic isolation of buildings, bridges or vibration-sensitive equipment [28]. For example, both the rubber-layer roller bearing (RLRB) system [29] and the rolling-ball rubber-layer (RBRL) system [30] comprise an array of steel balls interposed between flat surfaces covered with uniform rubber layers. Their rolling resistance can be simulated as a constant force model with a velocity-proportional transition at small velocities, while the rubber surface indentation effect caused by the ball pressure can be simulated as an additional nonlinear elastic spring model [31]. In [32], uniform elastomeric layers are proposed for non-concentric rolling isolation systems, to increase damping and ensure contact. In [33], a heavily-damped ball-in-cone device (BNC), made of a steel sphere rolling between uniform rubber-coated conical surfaces, is simulated through a rolling friction model, fitted to experimental tests. Rolling resistance is expressed by the product of a load-dependent friction force times a velocity-dependent transition law, while the indentation effect is modelled as a modification of the nominal rolling surface. In [34], a BNC variant is tested in which a geometric pattern is engraved on the rolling surface to increase friction. Texturing the surface slightly increases the rolling resistance but introduces undesired high-frequency acceleration components. Anyway, the engraved surface is still uniform in a macroscopic sense. In [35], a detailed theoretical model is developed for the RBRL system, depicting the insurgence, at the contact area between the rolling ball and the deformed rubber layer, of a slip region, characterized by a macroscopic sliding between the two materials. Again, uniform rolling surfaces are considered.

For a conventional BA, the disadvantage of a uniform rolling friction is that its equivalent damping ratio is inversely proportional to the amplitude of the ball displacement, and its effectiveness is amplitude dependent [36]. To avoid this inconvenient, following an idea originally presented in [37], Almazan et al. [38] invent a new type of hanging pendulum TMD, called the bidirectional and homogeneous TMD (BHTMD), in which a vertical friction damper is inserted between the pendular mass and the underlying structure. The first-order approximation of the resulting dissipative model turns out to be nonlinear but homogeneous, making both the equivalent damping ratio and the effectiveness of the device amplitude independent. To achieve the same result without recurring to a supplemental damper, Matta [39] proposes a new type of supported pendulum TMD, called the homogeneous tangential-friction bidirectional TMD (HT-BTMD), characterized by a tangential (rolling or sliding) friction varying along the pendulum surface

proportionally to the surface gradient. In [40], the HT-BTMD is shown to be more effective than the BHTMD if the pendulum surface is axial- or nearly-axial-symmetrical and if the absorber is bidirectionally excited.
Noticeably, unlike ball absorbers, both the BHTMD and the HT-BTMD are point-mass devices, i.e. characterized by a negligible rotational inertia.
In this paper, following the variable friction concept presented in [39], two new types of ball absorber are proposed as an alternative to the conventional uniform BA (UBA). The first type, called the homogeneous BA (HBA), is characterized by a rolling friction radially increasing in proportion to the ball angular displacement. Hardly realizable in practice, this friction model is nonlinear but homogeneous in the first order, where it ensures an amplitude-independent performance. The second type, called the discrete-homogeneous BA (DBA), is the discrete approximation of the HBA, characterized by a rolling friction radially increasing as a stepwise function of the angular displacement. Not exactly homogeneous, this friction model can be easily realized through juxtaposing multiple coating regions, with different thickness or material quality. For simplicity, the investigation is here confined to the assumption of a spherical rolling surface, although the concept could be applied in principle to any surface kind. With these premises, the following main points are addressed in the remainder of this work: (1) a unifying model is derived, valid for the three friction types (UBA, HBA and DBA) as well as for ideal viscous BAs (VBAs); (2) an optimal design procedure is formulated; (3) the results of experimental tests on small-scale prototypes of UBA and DBA are presented; (4) the results of numerical simulations of a real-scale case study are reported.

2. The analytical model

This section derives the fully nonlinear 3D model valid for viscous and friction BAs. The model is obtained for the BA alone and then augmented to include the main structure. Its first-order approximation is derived, which will be used in later sections to develop an optimal design methodology. The modelling framework, based on Gibbs-Appell nonholonomic formulation [41], is the one already adopted in [19], here focused on ball absorbers and extended to friction dissipation.

2.1 The kinematic equations

The model of a BA is schematized in Figure 2. It consists of a spherical ball of radius R, mass I and moment of inertia J around its centre of mass, which is subject to gravity g and rolls without sliding in a spherical cavity of radius L'. The cavity is integral with the structural support, supposed to translate without rotating. Denoting by O the at-rest position of the ball centre, and by u, v, and w the ball centre coordinates in the local Cartesian system xyz (centred in O and fixed to the structural support), the ball centre moves along the "virtual" spherical surface of radius $L = L' - R$ (in contradistinction with the "physical" cavity described by the contact point C), according to the kinematic holonomic constraint equation $h(u,v,w) = u^2 + v^2 + w^2 - 2Lw = 0$. Denoting by $\mathbf{n} = [n_x, n_y, n_z]^T = [-u, -v, L-w]^T / L$ the normal versor at the surface in C, and by $\mathbf{r} = [u,v,w]^T$ the ball centre relative displacement vector, the no-sliding condition is given by the following kinematic nonholonomic constraint equation:

$$\dot{\mathbf{r}} = \boldsymbol{\omega} \times R\mathbf{n} \tag{1}$$

which relates the ball centre relative velocity vector $\dot{\mathbf{r}} = [\dot{u}, \dot{v}, \dot{w}]^T$ with the ball angular velocity vector $\boldsymbol{\omega} = [\omega_x, \omega_y, \omega_z]^T$. Developing the right-hand side of Eq. (1), the three components of the relative velocity vector are obtained as

$$\dot{u} = R(\omega_y n_z - \omega_z n_y) \quad \dot{v} = R(\omega_z n_x - \omega_x n_z) \quad \dot{w} = R(\omega_x n_y - \omega_y n_x) \tag{2}$$

whence the three components of the relative acceleration vector $\ddot{\mathbf{r}} = [\ddot{u}, \ddot{v}, \ddot{w}]^T$ are derived as

$$\begin{aligned}\ddot{u} &= R\left(\dot{\omega}_y n_z - \dot{\omega}_z n_y + \omega_y \dot{n}_z - \omega_z \dot{n}_y\right)\\ \ddot{v} &= R\left(\dot{\omega}_z n_x - \dot{\omega}_x n_z + \omega_z \dot{n}_x - \omega_x \dot{n}_z\right)\\ \ddot{w} &= R\left(\dot{\omega}_x n_y - \dot{\omega}_y n_x + \omega_x \dot{n}_y - \omega_y \dot{n}_x\right)\end{aligned} \tag{3}$$

where $\dot{n}_x$, $\dot{n}_y$ and $\dot{n}_z$ are given by

$$\dot{n}_x = -\dot{u}/L \quad \dot{n}_y = -\dot{v}/L \quad \dot{n}_z = -\dot{w}/L \tag{4}$$

Finally, the absolute acceleration of the structural support is expressed by $\mathbf{a} = [a_x, a_y, a_z]^T$.

2.2 The dissipative model

In the absence of slippage, energy dissipation comes from rolling resistance, which results from the asymmetric pressure distribution arising at the interface between the ball and the physical surface, because of the viscoelastic deformations of the parts in contact [35]. Rolling resistance, in fact a resisting torque [42], is often modelled, in analogy with sliding friction and neglecting spinning friction, as a dissipative force acting on the centre of mass of the rolling body, in the opposite direction to its relative velocity. This dissipative force, conventionally called rolling friction (although no friction actually occurs), is generally expressed as the product of the normal contact force N times the rolling friction coefficient μ, whose value depends on several parameters, including the quality of the materials in contact, the value of the normal contact force, and the value of the relative velocity.

In this paper, rolling resistance is indeed modelled as such a kind of dissipative force, applied to the ball centre (i.e. tangent to the virtual surface) and defined by

$$\mathbf{f}_d = -f_d \mathbf{t} \tag{5}$$

where $\mathbf{f}_d = [f_{dx}, f_{dy}, f_{dz}]^T$ is the dissipative force vector, f_d is its modulus (called the dissipative force, for brevity), and $\mathbf{t} = [t_x, t_y, t_z]^T$ is the tangent versor to the relative motion of the ball centre, defined by $\mathbf{t} = \mathbf{0}$ if $\dot{\mathbf{r}} = \mathbf{0}$ and by $\mathbf{t} = \dot{\mathbf{r}}/\|\dot{\mathbf{r}}\| = [\dot{u}, \dot{v}, \dot{w}]^T/\|\dot{\mathbf{r}}\|$ elsewise. To jointly represent the various dissipative mechanisms later addressed in this study, the dissipative force in Eq. (5) is conveniently expressed as follows:

$$f_d = f_d(N, \theta, \|\dot{\mathbf{r}}\|) \tag{6}$$

where N is the modulus of the normal contact force vector $\mathbf{N} = N\mathbf{n}$, and θ is the ball angular displacement, defined as the positive angle between $\mathbf{n}$ and the z vertical axis (so that $n_z = \cos\theta$). For simplicity, the dissipative force in Eq. (6) is isotropic and memory-independent.

Eq. (6) is then specialized to represent four main dissipative models, respectively incorporated in the following BA types:

- Viscous BA (VBA), characterized by

$$f_d = f_d(\|\dot{\mathbf{r}}\|) = c\|\dot{\mathbf{r}}\| \tag{7}$$

where c is the viscous damping coefficient; combined with Eq. (5), Eq. (7) describes a force $\mathbf{f}_d = -c\|\dot{\mathbf{r}}\|\mathbf{t} = -c\dot{\mathbf{r}}$ that does not really correspond to any practical arrangement of viscous dashpots, but rather represents a somewhat ideal viscous damper, always oriented as the local tangent vector [43];

- Uniform friction BA (UBA), characterized by

$$f_d = f_d(N) = \mu_u N \tag{8}$$

where μ_u is the rolling friction coefficient, assumed uniform along the cavity;

- Homogeneous friction BA (HBA), characterized by

$$f_d = f_d(N,\theta) = \mu(\theta)N = \mu_0\theta N \tag{9}$$

where $\mu(\theta) = \mu_0\theta$ is the radially-varying rolling friction coefficient, assumed proportional to θ;

- Discrete-homogeneous friction BA (DBA), characterized by

$$f_d = f_d(N,\theta) = \mu(\theta)N = \mu_s(\theta)N \tag{10}$$

where $\mu_s(\theta)$ is the radially-varying rolling friction coefficient, assumed stepwise increasing with θ.

Of the four BA types introduced above, the VBA is the only one in which f_d depends on velocity. At low amplitudes, it coincides with the classical paradigm of a linear BA (LBA). In this paper, the VBA constitutes the ideal case of amplitude-independent damping, a useful benchmark to compare the performance of friction BAs rather than a commonly adopted, practical device.

The other three BA types, instead, implement a Coulomb friction model, in which f_d is the product of N and μ. However, while for the UBA μ is constant along the cavity, for the HBA and DBA μ radially varies along it, in either a continuous or discrete way. The HBA, in particular, applies to ball absorbers the concept of variable friction recently proposed for point-mass pendulum TMDs in [39], with some improvements. In fact, while the friction law adopted in [39] implies a proportional increase of μ with the surface gradient, resulting for a spherical pendulum in $\mu(\theta) = \mu_0 \tan\theta$, the friction law proposed here implies a proportional increase of μ with θ, i.e. $\mu(\theta) = \mu_0\theta$. The two laws tend to coincide as θ tends to 0, both ensuring a homogeneous first-order model (and thus an amplitude-independent performance), but the new law describes a more gradual increment of μ with θ, easier to realize in practice. Additionally, for an HBA obeying Eq. (9), it can be easily proven that: (i) as θ tends to 0, $\mu_0 < 1$ is necessary and sufficient condition for the re-centring of the device; (ii) otherwise, $\mu_0 < 1$ is sufficient but not necessary condition for its re-centring.

The three friction BAs are schematically shown in Figure 3. In principle, μ can be varied along the cavity by varying the quality or thickness of its coating. While the UBA represents a conventional BA with a uniform coating [18, 25-27], the HBA represents an ideal continuously varying coating, and the DBA represents its discrete approximation, obtained through juxtaposing multiple uniform coatings. Evidently, the UBA can also be seen as a single-step DBA.

Beyond the four dissipative models presented above, a variant of the UBA and the DBA will also be used in this paper, more suitable to match experimental tests. Accordingly, Eqs. (8) and (10) are modified as follows:

$$f_d = f_d(N,\|\dot{\mathbf{r}}\|) = \mu_u \tanh\left(\frac{\|\dot{\mathbf{r}}\|}{\|\dot{\mathbf{r}}\|_u^*}\right)N \tag{11}$$

$$f_d = f_d(N,\theta,\|\dot{\mathbf{r}}\|) = \mu_s(\theta)\tanh\left(\frac{\|\dot{\mathbf{r}}\|}{\|\dot{\mathbf{r}}\|_s^*(\theta)}\right)N \tag{12}$$

where $\|\dot{\mathbf{r}}\|_u^*$ and $\|\dot{\mathbf{r}}\|_s^*(\theta)$ are material-dependent reference velocities, and the hyperbolic functions express a smooth transition of the friction force across zero velocity, opposed to the rigid-plastic models of Eqs. (8) and (10) [33].

To completely define f_d in the above equations, N can be derived as follows. By applying Newton's second law to the ball mass m subject to its own weight $\mathbf{w} = [0,0,-mg]^T$, to the contact normal reaction force $\mathbf{N}$, and to the dissipative force f_d, the dynamic equilibrium equation is obtained as $\mathbf{w}+\mathbf{N}+\mathbf{f}_d = m(\mathbf{a}+\ddot{\mathbf{r}})$, where $\mathbf{a}+\ddot{\mathbf{r}}$ is the absolute acceleration of m. Denoting as

$$\boldsymbol{\lambda}_d = m(\mathbf{a} + \ddot{\mathbf{r}}) \tag{13}$$

the dynamic interaction force exchanged between the BA and its support, the same equation provides $\mathbf{N} = \boldsymbol{\lambda}_d - \mathbf{w} - \mathbf{f}_d$ and finally $N = m(\mathbf{a} + \ddot{\mathbf{r}})\mathbf{n} + mgn_z$.

2.3 The model of the ball absorber

Using Gibbs-Appell formulation, the analytical model of the BA can be derived as follows. First, the acceleration energy *S* of the BA is evaluated as

$$S = \frac{m}{2}[(\alpha_x + \ddot{u})^2 + (\alpha_y + \ddot{v})^2 + (\alpha_z + \ddot{w})^2] + \frac{J}{2}[\dot{\omega}_x{}^2 + \dot{\omega}_y{}^2 + \dot{\omega}_z{}^2] \tag{14}$$

and its portion S^* is retained, that only depends on the second derivatives of the nonholonomic quasi-coordinates, $\dot{\omega}_x$, $\dot{\omega}_y$, $\dot{\omega}_z$. Then, the elementary work done by nonconservative and gravitational forces against a virtual variation of the dynamic equilibrium position is computed as

$$\delta A = f_{dx}\delta u + f_{dy}\delta v + f_{dz}\delta w - mg\delta w \tag{15}$$

and eventually expressed in terms of the generalized forces P_{π_x}, P_{π_z}, P_{π_y} as

$$\delta A = P_{\pi_x}\delta\pi_x + P_{\pi_y}\delta\pi_y + P_{\pi_z}\delta\pi_z \tag{16}$$

where π_x, π_y, and π_z are the nonholonomic quasi-coordinates defined by $\dot{\pi}_x = \omega_x$, $\dot{\pi}_y = \omega_y$, $\dot{\pi}_z = \omega_z$.
At last, by substituting into Eq. (15) the elementary ball displacement components $\delta u = R(\delta\pi_y n_z - \delta\pi_z n_y)$, $\delta v = R(\delta\pi_z n_x - \delta\pi_x n_z)$, $\delta w = R(\delta\pi_x n_y - \delta\pi_y n_x)$, by comparing the result with Eq. (16), and by imposing the Gibbs-Appell equations as

$$\frac{\partial S^*}{\partial \dot{\omega}_x} = P_{\pi_x} \quad \frac{\partial S^*}{\partial \dot{\omega}_y} = P_{\pi_y} \quad \frac{\partial S^*}{\partial \dot{\omega}_z} = P_{\pi_z} \tag{17}$$

the following fully nonlinear model of the BA is finally obtained:

$$\begin{aligned}
&J\dot{\omega}_x + mR^2[(n_y^2 + n_z^2)\dot{\omega}_x - n_y n_x\dot{\omega}_y - n_z n_x\dot{\omega}_z + (n_y\dot{n}_y + n_z\dot{n}_z)\omega_x - n_y\dot{n}_x\omega_y - n_z\dot{n}_x\omega_z] = \\
&\quad = R(f_{dz}n_y - f_{dy}n_z) - mgRn_y + mR(a_y n_z - a_z n_y) \\
&J\dot{\omega}_y + mR^2[(n_z^2 + n_x^2)\dot{\omega}_y - n_z n_y\dot{\omega}_z - n_x n_y\dot{\omega}_x + (n_x\dot{n}_x + n_z\dot{n}_z)\omega_y - n_z\dot{n}_y\omega_z - n_x\dot{n}_y\omega_x] = \\
&\quad = R(f_{dx}n_z - f_{dz}n_x) + mgRn_x + mR(a_z n_x - a_x n_z) \\
&J\dot{\omega}_z + mR^2[(n_x^2 + n_y^2)\dot{\omega}_z - n_x n_z\dot{\omega}_x - n_y n_z\dot{\omega}_y + (n_x\dot{n}_x + n_y\dot{n}_y)\omega_z - n_x\dot{n}_z\omega_x - n_y\dot{n}_z\omega_y] = \\
&\quad = R(f_{dy}n_x - f_{dx}n_y) + mR(a_x n_y - a_y n_x)
\end{aligned} \tag{18}$$

The three scalar Eqs. (18), complemented with the kinematic equations (2) and (4), and with the constitutive equation (5), completely define the dynamic model of the BA.

2.4 The model of the ball absorber on an MDOF structure

The equation of motion of a linear multi-degree-of-freedom (MDOF) structure coupled with a BA and subjected to external forces and ground accelerations can be expressed as

$$\mathbf{M}_s\ddot{\mathbf{q}}_s + \mathbf{C}_s\dot{\mathbf{q}}_s + \mathbf{K}_s\mathbf{q}_s = \mathbf{f}_s - \mathbf{M}_s\mathbf{R}_s\ddot{\mathbf{r}}_g - \mathbf{L}^T\boldsymbol{\lambda}_d \tag{19}$$

where $\mathbf{q}_s$ is the vector of structural DOFs; $\mathbf{M}_s$, $\mathbf{C}_s$, and $\mathbf{K}_s$ are the structural mass, damping, and stiffness matrices; $\mathbf{f}_s$ is the external force vector; $\mathbf{R}_s$ is the input topological matrix; $\ddot{\mathbf{r}}_g = [\ddot{u}_g, \ddot{v}_g, \ddot{w}_g]^T$ is the ground

acceleration vector; $\mathbf{L}$ is a kinematic transformation matrix; and $\boldsymbol{\lambda}_d$ is the dynamic interaction force vector between the BA and its structural support. Recalling that $\boldsymbol{\lambda}_d$ is defined by Eq. (13) as $\boldsymbol{\lambda}_d = m(\mathbf{a} + \ddot{\mathbf{r}})$, where $\ddot{\mathbf{r}}$ is given by Eq. (3) and $\mathbf{a}$ is now given by

$$\mathbf{a} = \mathbf{L}(\ddot{\mathbf{q}}_s + \mathbf{R}_s \ddot{\mathbf{r}}_g) \tag{20}$$

it can be concluded that Eqs. (18) and (19), complemented with Eqs. (2) to (5) and with Eqs. (13) and (20), define the dynamic model of a linear MDOF structure equipped with a BA.

In particular, assuming for simplicity an N-story building with two lateral DOFs per story (along x and y) and a BA attached to the j^{th} story, and accordingly denoting by $\mathbf{u}_s$ and $\mathbf{v}_s$ the said lateral DOFs, by m_{si} the structural mass of the i^{th} story, by $\mathbf{C}_{sx}$, $\mathbf{C}_{sy}$, $\mathbf{K}_{sx}$ and $\mathbf{K}_{sy}$ the damping and stiffness matrices along x and y, and by $\mathbf{f}_{sx}$ and $\mathbf{f}_{sy}$ the external force vectors along x and y, then the equations of motion of the i^{th} story can be expressed, respectively along x and y, as follows:

$$\begin{aligned} m_{si}(\ddot{u}_g + \ddot{u}_{si}) + \mathbf{C}_{sxi}\dot{\mathbf{u}}_s + \mathbf{K}_{sxi}\mathbf{u}_s &= f_{sxi} - \delta_{ij} m(a_x + \ddot{u}) \\ m_{si}(\ddot{v}_g + \ddot{v}_{si}) + \mathbf{C}_{syi}\dot{\mathbf{v}}_s + \mathbf{K}_{syi}\mathbf{v}_s &= f_{syi} - \delta_{ij} m(a_y + \ddot{v}) \end{aligned} \tag{21}$$

where the subscript i denotes the i^{th} row of a vector or a matrix, and the topological operator δ_{ij} is 1 if $i = j$, and 0 otherwise. Eqs. (18) and (21) provide the equations of motion of the coupled system, with the support accelerations given by $a_x = \ddot{u}_g + \ddot{u}_{sj}$, $a_y = \ddot{v}_g + \ddot{v}_{sj}$, and $a_z = 0$, and with $\ddot{u}$ and $\ddot{v}$ given by Eqs. (3). Turning to a state space representation, Eqs. (18) and (21) can be transformed into a system of first-order nonlinear ordinary differential equations, and then numerically integrated by a Runge–Kutta algorithm, which in this paper is done using a MATLAB ODE solver [44].

2.5 The first-order model

Assuming low input and response amplitudes, the following first-order approximation of Eqs. (18) holds:

$$\begin{aligned} (J/R^2 + m)\ddot{u} - f_{dx} + mgu/L &= -ma_x \\ (J/R^2 + m)\ddot{v} - f_{dy} + mgv/L &= -ma_y \end{aligned} \tag{22}$$

where f_{dx} and f_{dy} are respectively given:

- for the VBA, according to Eq. (7), as

$$f_{dx} = -c\dot{u} \qquad f_{dy} = -c\dot{v} \tag{23}$$

- for the UBA, according to Eq. (8), as

$$f_{dx} = -\mu_u mgt_x \qquad f_{dy} = -\mu_u mgt_y \tag{24}$$

- for the HBA, according to Eq. (9), as

$$f_{dx} = -\mu_0 mgt_x\theta \qquad f_{dy} = -\mu_0 mgt_y\theta \tag{25}$$

- for the DBA, according to Eq. (10), as

$$f_{dx} = -\mu_s(\theta)mgt_x \qquad f_{dy} = -\mu_s(\theta)mgt_y \tag{26}$$

Eqs. (22) are uncoupled and linear if complemented with Eqs. (23) (VBA model); coupled, nonlinear and nonhomogeneous if complemented with Eqs. (24) (UBA model) or Eqs. (26) (DBA model); coupled and nonlinear but homogeneous if complemented with Eqs. (25) (HBA model). Consequently, at low amplitudes the BA effectiveness is amplitude independent for the VBA and the HBA, and amplitude dependent for the UBA and the DBA.

2.6 The first-order 2DOF model

To establish an optimal design method, two further simplifications are convenient. First, the motion is supposed to occur in one vertical plane, here taken with no loss of generality as the *xz* plane. Second, the structure is schematized as an SDOF system [1]. Eqs. (21) and (22) thus become

$$\begin{aligned} \ddot{u}_s + 2\zeta_{sx}\omega_{sx}\dot{u}_s + \omega_{sx}^2 u_s &= \bar{f}_{sx} - \ddot{u}_g - m_R(\ddot{u}_g + \ddot{u}_s + \ddot{u}) \\ \ddot{u} - \bar{f}_{dx} + \omega^2 u &= -(\ddot{u}_g + \ddot{u}_s)/(1+\kappa) \end{aligned} \tag{27}$$

where $\omega_{sx} = \sqrt{k_{sx}/m_s}$ is the structural circular frequency; $\zeta_{sx} = c_{sx}/(2\omega_{sx}m_s)$ is the structural damping ratio; $\bar{f}_{sx} = f_{sx}/m_s$ is the mass-normalized external force; $m_R = m/m_s$ is the BA mass ratio; $\kappa = J/(mR^2)$ is the BA inertia coefficient; ω is the BA circular frequency, defined by

$$\omega = \sqrt{g/[L(1+\kappa)]} \tag{28}$$

and $\bar{f}_{dx}$ is the normalized BA dissipative force, that is defined by

$$\bar{f}_{dx} = f_{dx}/[m(1+\kappa)] \tag{29}$$

and that can be expressed, according to Eqs. (23) to (26) and because $t_x = \mathrm{sgn}(\dot{u})$ and $\theta \approx |u|/L$, as

$$\bar{f}_{dx} = -2\zeta\omega\dot{u} \tag{30}$$

$$\bar{f}_{dx} = -\mu_u g\,\mathrm{sgn}(\dot{u})/(1+\kappa) \tag{31}$$

$$\bar{f}_{dx} = -\mu_0\omega^2\,\mathrm{sgn}(\dot{u})|u| \tag{32}$$

$$\bar{f}_{dx} = -\mu_s(|u|/L)g\,\mathrm{sgn}(\dot{u})/(1+\kappa) \tag{33}$$

for, respectively, the VBA, the UBA, the HBA and the DBA. In Eq. (30), the VBA viscous damping is introduced as $\zeta = c/[2\omega m(1+\kappa)]$.

Eqs. (30) to (33) are the unidirectional analogue of Eqs. (23) to (26). They represent a dissipative force that is always opposed to the absorber velocity, and whose modulus is respectively: (i) proportional to the BA velocity (VBA); (ii) constant (UBA); (iii) proportional to the BA displacement (HBA); (iv) and stepwise increasing with the BA displacement (DBA).

The first of the two Eqs. (27) is the classical equation of a linear SDOF structure coupled with an SDOF appendage. Its last right-hand side term is the inertial force of the appendage reacting on the structure. The second equation is the equation of a linear SDOF system subject to a base acceleration input, whose amplitude is, however, reduced 1+κ times with respect to the actual acceleration of the structural support. According to Eqs. (28) and (29), the same reduction affects ω^2 and $\bar{f}_{dx}$. In short, the ball rolling inertia J reduces, through the rolling coefficient κ, the extent of the structure-absorber interaction and therefore the BA efficacy, and at the same time the BA frequency and the BA equivalent damping ratio [18]. Obviously, κ depends on the mass distribution within the ball, and equals 0 for a point-mass sphere, 2/5 for a homogeneous sphere, 2/3 for a hollow sphere. If the model is used to simulate cylindrical bodies rolling on a cylindrical surface, other possible values of κ include 1/2 for a homogeneous cylinder, and 1 for a hollow cylinder.

Interestingly, Eqs. (27), (31), and (33) show that the UBA and the DBA remain inactive as long as the support acceleration $\ddot{u}_g + \ddot{u}_s$ does not exceed, respectively, $\mu_u g$ and $\mu_{s1} g$, having denoted with μ_{s1} the friction coefficient pertaining to the first coating region of the DBA.

3. The optimal design

In this section, based on the first-order 2DOF model derived in Section 2.6, an optimal design procedure is proposed for the four BA types. First, an H_∞ design method is presented for VBAs, UBAs and HBAs, ensuring the minimal worst-case steady-state structural response to harmonic excitations. Then, a procedure is established to identify the DBA that most closely approximates the optimal HBA. Because the first-order 2DOF model is only an approximation of the fully nonlinear model derived in Section 2.3, the proposed design procedure is truly optimal in the small-amplitude domain but only approximately optimal in the large-amplitude domain. The proposal of a design method which, accounting for geometric nonlinearity, should be optimal even in the large-displacement regime is not in the scope of this paper. However, the role of geometrical nonlinearities on BAs optimized in such an approximated manner will be properly accounted for in Sections 4 and 5, respectively on experimental and numerical bases.

3.1 The optimal design of VBAs, UBAs and HBAs

An optimal design procedure is here presented for VBAs, UBAs and HBAs. The combined structure-BA system is supposed to obey in each direction the 2DOF model described in Section 2.6. For simplicity, the structure is also admitted to have the same frequency and damping ratio along *x* and *y*, so that the same BA will be optimal in both directions. If this were not the case, either a suboptimal BA should be accepted in at least one direction, or a non-axial-symmetrical cavity should be adopted instead of the spherical one [19]. This circumstance is not in the scope of this paper.

Optimization is formulated as a classical H_∞ design problem. Its aim is to minimize the worst-case steady-state structural response to a harmonic input of unknown frequency, i.e. the H_∞ norm of an appropriate input-output transfer function (TF). The input amplitude is irrelevant for the VBA and the HBA, characterized by homogeneous models, but decisive for the UBA, its constant dissipative force making its transfer function amplitude dependent. For the three BA types, the procedure is thus formalized as follows. First, the design scenario is established by assigning (i) the input-output TF representative of the control objectives; (ii) only for the UBA, the design input amplitude; and (iii) the structural damping ratio ζ_{sx} (derived from experimental identification), the mass ratio m_R (based on cost-benefit expectations) and the inertia coefficient κ (dependent on the ball type). Then, the minimization of the H_∞ norm of the TF is obtained by optimizing the remaining two BA parameters, i.e. the frequency ratio $\omega_R = \omega/\omega_{sx}$ and, depending on the BA type, the damping ratio ζ (VBA), or the friction coefficient μ_u (UBA), or the friction ratio μ_0 (HBA). Namely, denoting with ω^* the input circular frequency, with $|TF(\omega^*)|$ the TF modulus (normalized so that its maximum is 1 for the uncontrolled structure), and with $R_\infty = \max|TF(\omega^*)|$ the response ratio, the optimization problem is formalized as follows:

(i) for the VBA:

$$R_{\infty opt} = \min_{\omega_R,\zeta} \max_{\omega^*} \left|TF(\omega^*)\right| = \min_{\omega_R,\zeta} R_\infty \Rightarrow \omega_{Ropt}, \zeta_{opt} \tag{34}$$

(ii) for the UBA:

$$R_{\infty opt} = \min_{\omega_R,\mu_u} \max_{\omega^*} \left|TF(\omega^*)\right| = \min_{\omega_R,\mu_u} R_\infty \Rightarrow \omega_{Ropt}, \mu_{uopt} \tag{35}$$

(iii) for the HBA:

$$R_{\infty opt} = \min_{\omega_R,\mu_0} \max_{\omega^*} \left|TF(\omega^*)\right| = \min_{\omega_R,\mu_0} R_\infty \Rightarrow \omega_{Ropt}, \mu_{0opt} \tag{36}$$

For the VBA and the HBA the optimal solution is amplitude independent, while for the UBA is not. For the UBA, however, because of the particular form of Eq. (31), $\bar{f}_{dx}$ is at the same time: (i) independent from the input amplitude; (ii) independent from the first optimization parameter, i.e. ω_R; and (iii) proportional to the second optimization parameter, i.e. μ_u. This circumstance favourably makes the UBA optimal frequency ratio, ω_{Ropt}, amplitude independent, and the UBA optimal friction coefficient, μ_{uopt},

amplitude proportional. Therefore, solving Eq. (35) for a single input amplitude solves the problem for any other input amplitude.

In Appendix A, Eq. (34) is solved for a variety of design scenarios, until deriving practical fitting formulas for optimizing VBAs under either force or ground acceleration input.

In the remaining of this subsection, Eqs. (34) to (36) are instead solved for only two design scenarios, i.e. adopting a force-to-displacement TF and assuming ζ_{sx} = 1%, m_R = 1%, and either κ = 0 (point mass, scenario 1) or κ = 0.4 (homogeneous sphere, scenario 2). For the VBA, the amplitude of the harmonic response, $|TF(\omega^*)|$, is computed in closed form, using Eq. (A.1) in Appendix A. For the UBA and HBA, instead, it is computed by points, i.e. simulating the nonlinear system separately under each harmonic input frequency, until stabilization of the response amplitude. For simplicity, a unit input amplitude is assumed. In all cases, the optimization problems expressed by Eqs. (34) to (36) are solved numerically, using a branch and bound search algorithm followed by a nonlinear least-square solver.

For the two said design scenarios, the results of the optimization are reported in Figure 4a and in Table 1. Figure 4a shows the optimal TFs obtained for the three BA types and for the two κ values. For each κ value, the three curves reach approximately the same maximum, representing the response ratio R_{opt}. Expectedly, R_{opt} is smaller for κ = 0 than for κ = 0.4, due to the reduced structure-absorber interaction caused by the BA rotational inertia. The curves are nearly identical for the VBA and the HBA, and favourably narrower for the UBA, which shows a better performance for frequencies just outside the resonance bandwidth.

The corresponding optimal parameters and response ratios are reported in Table 1. Regarding the VBA and the HBA, as observed in [40] for viscous and homogeneous point-mass pendulums, it is here confirmed, for both κ values, that: (i) the optimal frequency ratio, ω_{Ropt}, is closer to 1 for the HBA than for the VBA; (ii) the so-called HBA equivalent viscous damping, μ_{0opt}/π, is only slightly less than ζ_{opt} [40]; (iii) the optimal response ratio, R_{opt}, is very slightly lower for the HBA than for the VBA. Regarding the UBA, it is observed, for both κ values, that: (i) ω_{Ropt} is comprised between the ω_{Ropt} values obtained for, respectively, the VBA and the HBA; (ii) μ_{uopt}, because of its proportionality with the input amplitude $\bar{f}_{sx0}$, is conveniently expressed by the ratio $\mu_{uopt} g/[(1+\kappa)\bar{f}_{sx0}]$, which is amplitude independent; and (iii) R_{opt} is just slightly larger than for the VBA. In general, by comparing the results obtained for κ = 0 and κ = 0.4, it appears that: (i) ω_{Ropt} slightly increases with κ for the VBA and the UBA, whereas slightly decreases with κ for the HBA; (ii) for the three BA types, the optimal damping decreases by about 20% as κ increases from 0 to 0.4; (iii) for the three BA types, R_{opt} increases by about 14% as κ increases from 0 to 0.4. For the VBA, these trends perfectly fit into the more general trends described in Appendix A.

From Figure 4a and Table 1, it can be concluded that the three optimal BAs are substantially equivalent in their H_∞ performance, which moderately decreases with increasing κ.

Table 1. H_∞ optimal VBA, UBA and HBA under force input, for ζ_{sx} = 1%, m_R = 1% and either κ = 0 or κ = 0.4.

κ	Type	ω_{Ropt}	ζ_{opt}	$\frac{\mu_{uopt} g}{(1+\kappa)\bar{f}_{sx0}}$	$\frac{\mu_{0opt}}{\pi}$	R_{opt}
0.0	VBA	0.9886	0.0625	-	-	0.2274
	UBA	0.9906	-	7.496	-	0.2281
	HBA	0.9971	-	-	0.0619	0.2261
0.4	VBA	0.9902	0.0531	-	-	0.2597
	UBA	0.9917	-	6.079	-	0.2603
	HBA	0.9964	-	-	0.0528	0.2586

This substantial equivalence actually results from the similar amount of energy dissipated per cycle by the three optimal BAs. For κ = 0.4, Figure 4b shows the steady-state dissipative force-displacement loops of the three BAs, obtained applying to the structure a harmonic force input $\bar{f}_{sx}(t) = \bar{f}_{sx0}\sin(\omega_{sx}t)$ ($\bar{f}_{sx0}$ being here the amplitude for which the UBA is optimal). For convenience, the dissipative force $\bar{f}_{dx}(t)$ is normalized to $\bar{f}_{sx0}$, and the absorber relative displacement $u(t)$ is normalized to the static structural displacement $u_{s0} = \bar{f}_{sx0}/\omega_{sx}^2$. The three loops have a similar area, i.e. a similar cyclic energy dissipation, but different shapes, in fact elliptical, rectangular and triangular, for, respectively, the VBA, the UBA and the HBA. These differences, scarcely relevant if $\bar{f}_{sx0}$ is as presumed in design, become important otherwise. In fact, whereas the VBA and the HBA loops are invariant with $\bar{f}_{sx0}$, the UBA loops become thinner than optimal if $\bar{f}_{sx0}$ increases (underdamped absorber), and thicker than optimal if $\bar{f}_{sx0}$ decreases (overdamped absorber).

The effect is shown for κ = 0.4 in Figure 4c, where the UBA transfer function is computed for various scaling factors of the $\bar{f}_{sx0}$ value used for optimization. For a unit factor, the TF is the same already shown in Figure 4a. As the factors increase from 1 to 8, the UBA becomes increasingly underdamped, as revealed by the increasingly high TF resonance peaks. As the factors decrease from 1 to 1/8, the UBA becomes increasingly overdamped, until nearly stuck to the structure.

In conclusion, the design procedure provides optimal VBAs and HBAs which are substantially equivalent to each other and amplitude independent, and optimal UBAs whose performance strongly depends on the input amplitude, their optimality being achieved only when the input is the one assumed in design.

These conclusions have been obtained using an H_∞ design approach, aimed at minimizing the structural response to deterministic sinusoidal excitations. Alternatively, optimization might be carried out using an H_2 design approach, aimed at minimizing the expected root-mean-square (rms) structural response to a stationary random input. The same H_∞ and H_2 approaches have been recently compared by the author in [40], where they were used to optimize bidirectional point-mass pendulum TMDs of viscous or homogeneous friction types. They were shown to lead to similar optimal solutions, with the H_∞ option only slightly more robust than its H_2 counterpart. Because the system was nonlinear, the H_2 objective function, which for a linear system would be simply computed by solving a classical Lyapunov equation, was instead evaluated through Monte Carlo simulations, by averaging the rms response of the system to a sufficient number of realizations of the stochastic input process. The same H_2 procedure could be applied to BAs, probably confirming the main conclusions drawn above. This investigation is however left for future study.

3.2 The optimal design of DBAs

Still assuming the first-order 2DOF model, an optimal design procedure is here developed for DBAs. It consists in finding the DBA that best approximates, in energetic terms, the optimal HBA of equal mass and equal rolling coefficient, as obtained in Section 3.1. Namely, once the optimal HBA parameters ω_{Ropt} and μ_{0opt} are obtained from Eq. (36), the DBA optimal frequency ratio is posed as ω_{Ropt}, and the DBA optimal stepwise friction law $\mu(\theta) = \mu_s(\theta)$ is determined that most closely fits the optimal HBA friction law $\mu(\theta) = \mu_{0opt}\theta$, under given constraints on $\mu_s(\theta)$, regarding the number n of coating regions (i.e. of steps) and either their extension or their friction coefficient.

In fact, denoting by θ_{si} the value of θ delimiting the i^{th} region of the n-step DBA, and by μ_{si} the friction coefficient pertaining to that region, and introducing as

$$E(\theta) = 4\int_0^\theta f_d(N,\theta')L\,d\theta' = 4NL\int_0^\theta \mu(\theta')\,d\theta' \tag{37}$$

the steady-state cyclic energy dissipated by a BA oscillating with amplitude θ, and as $\overline{E}(\theta) = E(\theta)/(4NL)$ the corresponding normalized dissipated energy, that is expressed by

$$\overline{E}_0(\theta) = \int_0^{\theta} \mu_{0opt}\theta' d\theta' = \frac{1}{2}\mu_{0opt}\theta^2 \tag{38}$$

for the HBA, and by

$$\overline{E}_s(\theta) = \int_0^{\theta} \mu_s(\theta')d\theta' = \overline{E}_s(\theta_{si-1}) + \mu_{si}(\theta - \theta_{si-1}) \quad , \quad \theta_{si-1} \le \theta < \theta_{si} \, , \quad i = 1, \ldots, n \tag{39}$$

for the DBA, then the DBA parameters θ_{si} and μ_{si} are defined optimal if they make $\overline{E}_s(\theta)$ fit $\overline{E}_0(\theta)$ with a minimum mean square error over the entire coated surface (i.e. for $0 \le \theta \le \theta_{sn}$) or, equivalently, if they minimize the following objective function:

$$F_{ob} = \frac{\int_0^{\theta_{sn}} [\overline{E}_s(\theta'') - \overline{E}_0(\theta'')]^2 d\theta''}{\int_0^{\theta_{sn}} \overline{E}_0(\theta'')^2 d\theta''} = \frac{20}{\mu_{0opt}^2 \theta_{sn}^5} \int_0^{\theta_{sn}} [\overline{E}_s(\theta'') - 1/2\mu_{0opt}\theta''^2]^2 d\theta'' \tag{40}$$

under certain constraints on n, θ_{si}, and/or μ_{si}.

The first constraint regards the choice of a reasonable value of n. For $n = 1$ the DBA degenerates into a UBA, for $n \to \infty$ into an HBA. Evidently, the larger is n, the more accurate is the fitting.

If $n = 1$, F_{ob} in Eq. (40) becomes

$$F_{ob} = \left[1 - 5\left(\frac{\mu_{s1}}{\mu_{0opt}\theta_{s1}} \right) + \frac{20}{3}\left(\frac{\mu_{s1}}{\mu_{0opt}\theta_{s1}} \right)^2 \right] \tag{41}$$

and its minimization provides the following closed-form optimal relation among μ_{0opt}, μ_{s1} and θ_{s1}:

$$\mu_{s1} = \frac{3}{8}\mu_{0opt}\theta_{s1} \tag{42}$$

If μ_{0opt} is assigned, Eq. (42) either provides μ_{s1} for a given θ_{s1}, or θ_{s1} for a given μ_{s1}. Recalling that the 1-step DBA is in fact a UBA, the proportional relation between μ_{s1} and θ_{s1} expressed by Eq. (42) confirms the one found between μ_{uopt} and $\bar{f}_{sx0}$ in Section 3.1.

Eq. (42) is used in Figure 5, where the optimal HBA and its best fitted 1-step DBA are compared, in terms of, respectively, their friction laws $\mu(\theta)$ (Figure 5a) and their normalized dissipated energies $\overline{E}(\theta)$ (Figure 5b). The design can proceed in two ways, depending if either θ_{s1} is assigned ("direct" approach) or μ_{s1} is assigned ("inverse" approach), as it will be better explained next for $n > 1$. In either way, μ_{s1} is 3/8 times the maximum friction coefficient $\mu_{0opt}\theta_{s1}$ reached by the HBA in θ_{s1} (Figure 5a), and $\overline{E}_s(\theta)$ is only a rough approximation of $\overline{E}_0(\theta)$ (Figure 5b), with the 1-step DBA clearly overdamped for $\theta < 3/4 \cdot \theta_{s1}$, and underdamped for $\theta > 3/4 \cdot \theta_{s1}$.

If $n > 1$, F_{ob} in Eq. (40) can be easily minimized numerically. Although other design approaches are possible, two main cases are here considered, each constituting an n-dimensional optimization problem:

(i) the "direct" approach: given the n values of θ_{si}, find the n values of μ_{si} which minimize F_{ob};

(ii) the "inverse" approach: given the n values of μ_{si}, find the n values of θ_{si} which minimize F_{ob}.

The direct approach is conceptually and computationally simpler, and useful for a preliminary design. For example, θ_{sn} can be assigned as the maximum angular stroke expected for the optimal HBA, and the other θ_{si} as evenly distributed between 0 and θ_{sn}, according to $\theta_{si} = i\theta_{sn}/n$. Under these assumptions, the optimal solution is shown in Figure 6 for n = 5. With respect to the 1-step DBA of Figure 5, the 5-step DBA clearly ensures a much better fitting of $\overline{E}_0(\theta)$ (Figure 6b), achieved through an uneven distribution of μ_{si}, comprised between $\mu_{s1} \approx 0.079\mu_{0opt}\theta_{s1}$ and $\mu_{sn} \approx 0.888\mu_{0opt}\theta_{sn}$ (Figure 6a). Intuitively, while for n = 1 the optimum is $\mu_{s1} = \mu_{sn} = 0.375\mu_{0opt}\theta_{sn}$, for $n \to \infty$ the optimum is $\mu_{s1} \to 0$ and $\mu_{sn} \to \mu_{0opt}\theta_{sn}$ (implying also $F_{ob} \to 0$). In general, the direct approach simulates the preliminary stage of a DBA design, through which the ideal desired friction coefficients are determined, based on the expected BA strokes. Its solution may be used to identify the most appropriate candidates of coating materials, or instead to exclude the feasibility of a DBA application, when the resulting friction coefficients were in fact unrealistic. In any case, the obtained optimal μ_{si} are unlikely to exactly match the friction coefficients of the available coating materials.

On the other hand, the inverse approach simulates the constructive stage of a DBA design, in which the coating regions are optimally tailored depending on the friction coefficients of the selected materials. The inverse approach is more complex than the direct approach, because θ_{sn} is both a design variable and the upper bound of the interval over which fitting is enforced. If the adopted μ_{si} are far from the theoretical values provided by the direct approach, then θ_{sn} will be far from the expected angular stroke. If, in particular, the adopted μ_{si} are lower than desired, fitting will be optimal only for BA excursions up to θ_{sn} : for larger excursions, supposing the coating remains the same as in the n^{th} region and no other dissipation mechanism intervenes (e.g. an end buffer), then the DBA will be underdamped.

In the remaining of this paper, the inverse design approach will be applied twice: first, in Section 4, to the real design of a DBA (for n = 3); then, in Section 5, to the simulated design of a DBA (for n = 5). For better clarity, the results of the first application are here anticipated in Table 2 and in Figure 7. According to the inverse approach, based on the known values of μ_{0opt} (here equal to 0.1421, see Section 4) and μ_{si} (see Table 2, column 3), the optimal θ_{si} are determined (Table 2, column 5). Comparing Figure 7 with Figures 5 and 6, an intermediate fitting accuracy is obtained, due to the intermediate value adopted for n. Because the optimal $\theta_{sn} = \theta_{s3}$ is only 0.525 rad (30.1°) while the DBA is to be tested under larger strokes, the outer region is extended beyond that value, up to 0.873 rad (50°). Clearly from Figure 7, the DBA will be underdamped in this extra region. The study of possible countermeasures, such as the incorporation of an end buffer to increase damping, is not in the scope of this paper.

Table 2. Coating features of the 3-step DBA prototype designed in Section 4.

n	*Type*	μ_{si} (‰)	$\|\dot{\mathbf{r}}\|^*_{si}$ (mm/s)	θ_{si} (rad)
1	Material 1	12.4	15	0.182
2	Material 2	34.0	25	0.322
3	Material 3	59.0	40	> 0.525

4. Experimental testing

To demonstrate the applicability of the homogeneous friction concept to ball absorbers, a small-scale prototype of DBA is built and tested on a cantilever tubular structure, and compared with a similar prototype of UBA. After preliminary experiments of the uncontrolled structure, the two prototypes are first tested in fixed-support conditions, for design and identification, and then on the structure in free- and

forced-vibration conditions, for performance evaluation. The tubular structure loosely represents a tower-like structure or an antenna.

4.1 Preliminary testing of the uncontrolled structure

4.1.1 Setup description

A general view of the experimental setup is shown in Figure 8. The structure is a steel vertical cantilever beam, having a tubular section with external diameter of 20 mm and thickness of 1 mm, and a total height of 1200 mm. Its lowest section is welded to a steel plate (100x100x8 mm^3) that is glued to a rigid steel pedestal (360x360x50 mm^3), on its turn bolted to the upper face of a small unidirectional shaking table. An assemblage of 12 steel plates, each 100x100 mm^2 wide and 5 or 6 mm thick (for a total thickness of 68 mm), with a central circular hole with diameter of 20 mm, is inserted on the tubular structure, at a distance of 71 mm from its top. On top of the structure, a removable hemispherical plastic cap is mounted through a steel tubular segment, glued to the cap and coaxially fitted to the tubular beam. The cap is made of transparent PVC, has internal radius of 57.75 mm and thickness of 1.75 mm. A triaxial accelerometer is attached onto the shaking table (S_1), and another onto the top of the plate assemblage (S_2). The significant masses are: 560 g for the tubular structure, 5020 g for the plate assemblage, 130 g for the DBA cap (included the mass of the rubber coating, as detailed next), and 30 g for the accelerometer.
The *xyz* reference coordinate system is oriented as follows: *x* in the shaking direction, *y* in the transverse direction, *z* in the vertical direction. The accelerometers and the plate assemblage are oriented accordingly, while the pedestal is rotated around *z* in such a way that the two principal structural modes (having not exactly coincident frequencies because of the inevitable geometrical imperfections) are parallel to *x* and *y*.
Visible in Figure 8a but irrelevant in this experiment, a second tubular beam is mounted on the same pedestal. Its frequency is so high and the pedestal so rigid that its dynamics are uncoupled from those of the system under study, and can be neglected.

4.1.2 Testing program

The system described above, with no ball in the hemispherical cap, represents the uncontrolled structure. For convenience, the masses of the cap and of the accelerometer S_2 are included in it.
The uncontrolled structure is dynamically identified through preliminary free- and forced-vibration tests. The identified frequency and damping of the structural target mode are required to trigger the BA design procedure. They are also used to calibrate the amount and position of the plate assemblage so to achieve a fine tuning of the absorber (in a real application, tuning would be achieved by changing the radius *L* of the virtual rolling surface).

4.1.3 Results

Several free- and forced-vibration tests are repeated on the uncontrolled structure. In Figure 9 the results of a free-vibration test are reported. An initial displacement is imposed to the top of the structure in the *x* direction and, after release, the free top acceleration along *x*, a_x, is measured by S_2. The time history, $a_x(t)$, is shown in Figure 9a for a duration of 600 s, and the modulus of its Fourier transform, $|A_x(\omega^*)|$, in Figure 9b. Also, the time-frequency spectrogram of $a_x(t)$ is shown in Figure 9c [44], while the instantaneous equivalent structural damping ratio ζ_{sx}, obtained through the logarithmic decrement method, is shown in Figure 9d, as a function of the instantaneous acceleration amplitude a_x^*. Figure 9c indicates that the natural frequency of the target mode, ω_{sx}, is constant with time and therefore with the response amplitude, while Figure 9d shows that its damping ratio is amplitude dependent (in the range 0.3÷4.0‰).
By averaging the results of several tests, frequencies and damping ratios are finally identified for the two uncontrolled fundamental modes as $\omega_{sx} = 2\pi \cdot 1.981$ rad/s, $\omega_{sy} = 2\pi \cdot 1.993$ rad/s, and $\zeta_{sx} \approx \zeta_{sy} \approx 1‰$. Through calibrating a finite element model of the uncontrolled structure (details here omitted for brevity), the effective mass of these fundamental modes, defined according to Warburton as a function of the

absorber attachment point [1], is m_s = 4255 g, i.e. equal to 74% of the total structural mass. The structure is basically a SDOF system (the experimental and simulated natural frequencies of the second flexural modes along *x* and *y* are around 53 Hz), and m_s is not a larger percentage of the total structural mass, mainly because the mass of the plate assemblage is located 105 mm below the absorber attachment point.

4.2 Design, construction and testing of the UBA and DBA prototypes

After the identification of the uncontrolled structure, the ball absorbers can be designed and constructed. The DBA prototype is designed as explained in Section 3.2, starting from the design of the optimal HBA. The UBA prototype is obtained by extending to the entire rolling surface the intermediate coating material of the DBA prototype.

4.2.1 HBA optimal design

According to Section 3.1, the optimal HBA is designed by numerically solving Eq. (36), assuming as the TF input the ground acceleration instead of the applied force, coherently with the way the excitation will be imparted in shaking-table tests.

A stainless steel homogeneous sphere is chosen as the rolling ball, having radius R = 10 mm, mass m = 32.9 g, and inertia coefficient κ = 0.4. With the target mode having an effective mass m_s = 4255 g, the mass ratio is therefore m_R = 0.7728 ≈ 0.77%. For m_R = 0.77%, ζ_{sx} = 1‰ and κ = 0.4, the optimal HBA parameters are ω_{Ropt} = 0.9964 and μ_{0opt} = 0.1421. Noticeably, the simplified VBA formulas in Appendix A, combined with the friction-viscous equivalence formulation, would provide $\mu_{0opt} \approx \pi\zeta_{opt}$ = 0.1433, which is very close to the exact numerical optimum.

4.2.2 Preliminary DBA optimal design (direct design approach)

Once the optimal HBA is determined, its frequency and friction ratios respectively provide the dimensions and the friction properties of the DBA rolling surface.

Regarding the surface dimensions, and focusing on the *x* direction, the structural frequency $\omega_{sx} = 2\pi \cdot 1.981$ rad/s and the optimal frequency ratio ω_{Ropt} = 0.9964 imply the absorber optimal frequency $\omega = 2\pi \cdot 1.9739$ rad/s, and consequently the optimal virtual radius L = 45.54 mm and the optimal physical radius $L' = L + R$ = 55.54 mm. Considering that the internal radius of the adopted PVC cap is 57.75 mm, the optimal coating thickness turns out to be 57.75-55.54 = 2.21 mm. In the *y* direction, where $\omega_{sy} = 2\pi \cdot 1.993$ rad/s, the same procedure gives L' = 54.67 mm, and therefore an optimal coating thickness of 3.08 mm.

Regarding the surface friction properties, the direct design approach explained in Section 3.2 allows for a rough estimation of the desired range of friction coefficients. For example, assuming θ_{sn} = 30° = 0.5236 rad as the maximum expected angular stroke, and still letting undefined the number n of coating regions, μ_{0opt} = 0.1421 would imply: for n = 1, a unique coating region with $\mu_{s1} = 0.375\,\mu_{0opt}\theta_{s1}$ = 27.9‰; for n = 5, five coating regions with μ_{si} ranging from $\mu_{s1} \approx 0.079\,\mu_{0opt}\theta_{s1}$ = 5.9‰ to $\mu_{sn} \approx 0.888\,\mu_{0opt}\theta_{sn}$ = 66.1‰.

4.2.3 Experimental characterization of possible coating layers

After preliminary tests here not discussed for brevity, four materials are selected as possible candidates for coating:

- material 0: PVC-coated ordinary adhesive tape, 0.13 mm thick;
- material 1: styrene-butadiene rubber layer, 2.0 mm thick;
- material 2: adhesive closed-cell EPDM sponge rubber layer, 2.6 mm thick;
- material 3: adhesive net-reinforced closed-cell foamed rubber layer, 2.7 mm thick.

Correspondingly, four UBA prototypes are built, each consisting of (i) a PVC hemispherical cap identical to the one described above, (ii) one layer of the respective material adhered to its inner surface, and (iii)

one steel ball, of variable diameter. Every UBA, its base being anchored to a fixed support, is then subjected to free-vibration tests, conducted by releasing the ball from an initial displaced position. By keeping the initial ball velocity at a minimum, the ball motion is ideally contained in a vertical plane (with no loss of generality, the *xz* plane), which permits to reduce the coated surface to a sufficiently large stripe, centred on that plane. In each test, the ball trajectory is recorded from above by a video camera aligned on the cap vertical axis, at a height of 220 mm on the cap equator. The camera acquires 2MP frames at 25 fps. To enhance contrast between the ball and the cap, and between the cap and the background, because the four materials are black or dark grey, the ball is painted white, and the cap surface that would be uncoated is covered with black tape. The video is processed using MATLAB's Image Processing Toolbox [44]. An appropriate nonlinear map is determined from pixel coordinates to physical coordinates, accounting for the varying distance of the ball from the camera during oscillations. As a result, each video provides the time-history $u(t)$ of the ball horizontal displacement along x, sampled at 25 Hz.

Tests are conducted for each material using three different ball radii, i.e. R = 10, 12.5, and 15 mm. For each combination of material and radius, tests are repeated several times to improve data consistency. For example, Figure 10 refers to the combination of material 2 and radius R = 10 mm. Figure 10a shows a picture of the tested cap. Figure 10b shows 6 consecutive frames after processing, with the fitting circles identifying the relative location of the ball and the cap equator. Figure 10c shows the resulting ball time response, after the nonlinear mapping application.

Then, for each combination of material and ball radius, the experimental ball response is fitted using the fully nonlinear BA model derived in Section 2.3, with the UBA friction law defined by Eq. (11) to account for the velocity-dependent friction transition across zero velocity. All modelling parameters are set to equal their nominal value, except for the friction coefficient μ_u and the reference velocity $\|\dot{\mathbf{r}}\|_u^*$, which are calibrated on the experiment. Figure 11 compares the experimental and simulated ball displacement time-histories obtained after fitting, for the four materials and for R = 10 mm. Table 3 reports the average values of the fitting parameters μ_u and $\|\dot{\mathbf{r}}\|_u^*$, after repeated testing. Both friction parameters progressively increase from material 0 to 3, showing instead limited variations with the ball radius.

Table 3. Experimentally fitted UBA friction parameters as a combination of material and ball radius.

Material	R (mm)	μ_u (‰)	$\|\dot{\mathbf{r}}\|_u^*$ (mm/s)
0	10.0	5.9	1.5
	12.5	4.7	1.5
	15.0	5.3	1.5
1	10.0	12.4	15
	12.5	11.7	15
	15.0	12.4	15
2	10.0	34.0	25
	12.5	32.2	30
	15.0	32.5	30
3	10.0	59.0	40
	12.5	53.0	40
	15.0	47.5	47

4.2.4 DBA optimal design (inverse design approach) and manufacturing

With the friction properties experimentally identified above, the DBA prototype can be designed using the inverse approach explained in Section 3.2. As anticipated in Section 4.2.1, the design is conducted assuming a 10mm-radius ball, in fact the only one that will be tested on the structure. For constructive reasons, material 0 is finally discarded, because its sensibly lower thickness would require a modification

of the shape of the uncoated cavity [39], here excluded. Therefore, only materials 1 to 3 are used. The results of the design procedure are reported in Table 2 and in Figure 6, and have already been commented in Section 3.2. The friction properties in Table 2, columns 3 and 4, are those reported in Table 3 for materials 1 to 3 and for R = 10 mm. The angles delimiting each region are reported in column 5. To account for extra strokes, material 3 is extended beyond θ_{s3}, up to 0.873 rad (50°).

The resulting 3-step DBA prototype is shown in Figure 12a, together with the UBA prototype coated with material 2. These are the only two BAs that will be tested on the structure. The DBA is manufactured by juxtaposing the three material layers, adhered to the cap surface through the interposition of additional adhesive tapes, meant to compensate for the different thickness of the three layers. The resulting uniform thickness of the DBA coating is about 3.0 mm. Because tests will be unidirectional, the UBA coating is made, for simplicity, of a single rubber stripe, centred on the plane of motion, and conservatively prolonged until $\theta_u \approx 60°$. To reproduce the complexity of a real design, the DBA coating is instead arranged in three-dimensions.

Figure 12b compares the free experimental response of the DBA (with R = 10 mm), obtained as described above for the UBAs, with the corresponding simulated response, computed using the fully nonlinear model derived in Section 2.3, with the DBA friction law being defined by Eq. (12). The friction parameters are given in Table 2, the other parameters are taken as nominal. In dotted blue line, the simulated response is also reported for the ideal optimal HBA. A good correspondence exists between the experimental and the simulated DBA responses, although the experimental response appears slightly more damped, probably because of the unavoidable irregularities in between adjacent regions. A satisfactory agreement is also observed between the DBA and the HBA responses, except at small displacements, where the DBA proves expectedly more damped.

4.3 Experimental testing of the structure coupled with the UBA and DBA prototypes

Finally, the UBA and DBA prototypes (Figure 12a, with R = 10 mm) are mounted on the structure, and free- and forced-vibration tests are performed on the coupled system, by imparting along x either an initial displacement of the top of the structure or a unidirectional acceleration of its pedestal.

The results of free-vibration tests are reported in Figure 13. 21 tests are shown for the UBA-controlled structure (black and green curves), and 21 tests for the DBA-controlled structure (red curves). For the 42 tests, Figure 13a shows the first 20 seconds of the top acceleration time-histories $a_x(t)$; Figure 13b shows, for better clarity, the time-histories of the instantaneous acceleration amplitudes; and Figure 13c shows the instantaneous equivalent viscous damping ratio as a function of the acceleration amplitude, computed with the logarithmic damping method. In fact, Figures 13a and 13c are the controlled analogues of Figures 9a and 9d. Depending on the imparted initial displacement, the maximum acceleration amplitudes at the beginning of the records vary between 0.23 m/s^2 and 1.36 m/s^2 for the UBA, and between 0.22 m/s^2 and 0.92 m/s^2 for the DBA. Larger amplitudes resulted in the ball exiting the rubber coating, so the relative tests are not reported. Despite the apparently identical testing conditions, the UBA-controlled structure exhibits two distinct behaviours, highlighted in different colours. In 11 of the 21 tests (black curves), the UBA activates as expected: the structural response gets reduced in a few seconds until reaching a threshold acceleration amplitude of about 0.20 m/s^2, after which the ball relative motion gets practically annulled, and the structure oscillates as if uncontrolled. Accordingly, the equivalent damping ratio gets as high as 25÷40‰ during the first instants of motion, dropping to about 1‰ in the virtually uncontrolled regime (in agreement with Figure 9). In the remaining 10 tests (green curves), unexpectedly, the UBA does not activate, and the structure oscillates from the beginning as if uncontrolled, with an equivalent damping ratio progressively decreasing from 2‰ to 1‰. This remarkable difference, not clearly related with the initial displacement amplitude (three black curves have a lower initial amplitude than most green curves), nor with the order of testing (green curves correspond to tests #1÷3, 5, 7, 9, 11, 14, 15, 21, and the time between two successive tests have been kept constant), might be attributed to not perfectly zero velocity initial conditions, thus reflecting some kind of chaotic behaviour, whose investigation is however left for future work. As far as the DBA is concerned (red curves), instead, the absorber activates in all 21

tests, as for the black UBA curves. The equivalent damping ratio, however, is increased up to 40÷70‰, and the threshold acceleration amplitude is favourably reduced to 0.07 m/s^2, thus demonstrating the superior effectiveness of the DBA over the UBA device. Noticeably, the two threshold acceleration amplitudes are in good agreement with the friction parameters identified in Tables 2 and 3. In the assumption of a dry-friction model, those thresholds would equal $\mu_u g$ = 0.33 m/s^2 for the UBA, and $\mu_{s1} g$ = 0.12 m/s^2 for the DBA (see again Section 2.6). The respective experimental values, 0.20 m/s^2 and 0.07 m/s^2, are about 40% lesser, coherently with the identified smooth transition law, that reduces friction at small velocities.

Finally, the results of forced-vibration tests are reported in Figure 14. A unidirectional random base acceleration is imparted through the shaking table to the structure, in either uncontrolled or controlled conditions, and the corresponding linearized input-output TF is computed from sensor S_1 to sensor S_2. Tests are repeated for increasing levels of shaking, each test lasting 600 s. The rms of each base acceleration time-history is reported in the figure legend, expressed in cm/s^2, ranging from 2.0 to 9.8 cm/s^2. The green curve refers to the uncontrolled structure, the black and the red curves refer to, respectively, the UBA- and the DBA-controlled structure. In the presence of the UBA, the TFs significantly vary with the input level, their peak value ranging from 181 (for a rms of 2.0 cm/s^2) to 31 (for a rms of 6.2 cm/s^2). In the presence of the DBA, the TFs appear flat for any input level (with their peak ranging from 22 to 31), except for the lower level (rms = 2.0 cm/s^2), when the TF peak increases to 60, probably because the ball motion is in this case confined to the inner coating region, in fact experiencing a uniform friction. These results confirm the superior and substantially amplitude-independent performance of the DBA prototype, also suggesting that further improvements could be obtained including material 0 too into the surface coating.

5. Numerical case study: wind mitigation of the Nagasaki Airport Tower

The Nagasaki Airport Tower is a wind-sensitive building, on which tuned liquid sloshing dampers (TLSD) were temporarily installed in the '80s to reduce wind-induced vibrations [45, 46]. This section simulates the wind response of the Nagasaki Airport Tower, comparing the uncontrolled case with five alternative controlled cases, each corresponding to a different type of ball absorber, namely the LBA, the VBA, the HBA, the DBA, and the UBA, this latter proposed in three different variants. Because the tower is modelled as a linear MDOF structure, the uncontrolled case and the LBA-controlled case admit the linear model given by Eqs. (21) and (22), whereas the remaining four controlled cases are described by the fully nonlinear model expressed by Eqs. (18) and (21). Obviously, the LBA and the VBA cases coincide as long as the device works in the low-amplitude domain.

5.1 The structure

The structural model of the Nagasaki Airport Tower is based on the description provided in [45, 46]. The tower is a 42 m tall, steel-framed, doubly-symmetrical building. It consists of a 38.5 m tall tower (having a 5.15 m x 5.15 m square section), and of a 3.5 m tall air-traffic control room placed on top of it (having a 7.40 m x 7.40 m square section). The total mass of the tower is $1.7 \cdot 10^5$ kg. Its fundamental vibration modes along *x* and *y* have identical natural frequencies of 1.07 Hz and damping ratios of about 0.9%. A TLSD system was installed in the control room for two weeks in 1987. It consisted of an assembly of 25 cylindrical multi-layered vessels partially filled with water, having a total mass of 950 kg tuned to the fundamental modes. Rms response reductions of about 50% were observed under medium wind velocities. Based on data regression, it was estimated that the uncontrolled tower would exceed the acceleration limits provided by several international codes, instead achieving full conformity in the presence of the TLSD system.

In this paper, the tower is modelled as a 12-element cantilever Euler-Bernoulli beam, identical in the two directions, with constant flexural stiffness along the height and with variable mass, lumped at the nodes. Main modelling data are summarized in Table 4. The first three modes in each direction have natural frequencies of 1.07 Hz, 7.73 Hz and 22.47 Hz, and participating masses of 67.7%, 17.9% and 5.9%. Damping ratio is assumed at 1% in every mode.

Table 4. Main structural data of the numerical model of the Nagasaki Airport Tower.

Node number (-)	Height above the ground (m)	Mass ($kg \cdot 10^3$)	Flexural stiffness ($Nm^2 \cdot 10^{10}$)	Cross-section average side (m)	Tributary wind area (m^2)
1	3.5	12.0	7.00	5.15	18.03
2	7.0	12.0	7.00	5.15	18.03
3	10.5	12.0	7.00	5.15	18.03
4	14.0	12.0	7.00	5.15	18.03
5	17.5	12.0	7.00	5.15	18.03
6	21.0	12.0	7.00	5.15	18.03
7	24.5	12.0	7.00	5.15	18.03
8	28.0	12.0	7.00	5.15	18.03
9	31.5	12.0	7.00	5.15	18.03
10	35.0	12.0	7.00	5.15	18.03
11	38.5	30.0	7.00	6.28	21.96
12	42.0	20.0	7.00	7.40	12.95

5.2 The ball absorber

The absorber is supposed to be a steel homogeneous sphere rolling without sliding in a spherical container, attached to the roof of the control room (node #12 in the structural model). The ball radius R is taken as 300 mm, as in the prototype designed by Pirner [18]. Consequently, the ball mass is m = 888 kg, equal to 0.52% of the mass of the tower, and slightly less than the mass of the TLSD system installed in 1987. According to Warburton's approach [1], the corresponding effective mass ratio is m_R = 1.40% in both directions.

For the VBA and the HBA, the frequency and damping ratio are obtained through the design procedure explained in Section 3.1, adopting m_R = 1.40% and ζ_{sx} = 1.0%. They are reported in Table 5, together with the corresponding pendulum frequency and main dimensions. For the VBA type, ω_R and ζ are very close to those provided by Eqs. (A.3) and (A.4) in Appendix A (with an error of 0.3‰ in frequency and 10‰ in damping). Also, μ_0 / π is only slightly less than ζ, which confirms what obtained in Section 3.1 (Table 1), and shows the usability of those fitting formulas as an approximate design tool for HBAs too.

Table 5. VBA and HBA parameters.

Type	ω_R (-)	ζ (-)	μ_0 / π (-)	$\omega/(2\pi)$ (Hz)	L (mm)	L' (mm)
VBA	0.9865	0.0628	-	1.0556	159.2	459.2
HBA	0.9951	-	0.06163	1.0648	156.5	456.5

For the DBA, ω_R, L, and L' are the same as for the HBA, but instead of the continuous friction pattern, n = 5 coatings are assumed, characterized by friction coefficients μ_{si} ranging from 5‰ to 90‰, and by a very small uniform reference velocity $\|\dot{\mathbf{r}}\|_{si}^* = \|\dot{\mathbf{r}}\|_s^* = 0.1$ mm/s. Details are reported in Table 6, columns 3 and 4. Column 5 reports the corresponding θ_{si} values, obtained through the inverse design approach explained in Section 3.2. In fact, $\mu = \mu_{s5}$ is assumed also for $\theta > \theta_{s5}$.

For the UBA, ω_R, L, and L' are also the same, but only a single coating is assumed on the rolling surface. As reported in Table 6, three options are considered, denoted as UBA-1, UBA-2 and UBA-3, wherein μ_u respectively equals the DBA friction coefficients μ_{s2}, μ_{s3}, and μ_{s4}, and $\|\dot{\mathbf{r}}\|_u^*$ equals $\|\dot{\mathbf{r}}\|_s^*$.

For better clarity, the HBA, the DBA and the three UBA options are compared in Figure 15, in terms of friction laws and dissipated energies.

Table 6. DBA and UBA parameters.

Type	ω_R (-)	μ_{si} , μ_u (‰)	$\left\|\dot{\mathbf{r}}\right\|_{si}^*$, $\left\|\dot{\mathbf{r}}\right\|_u^*$ (mm/s)	θ_{si} (rad)	$\omega/(2\pi)$ (Hz)	L (mm)	L' (mm)
DBA	0.9951	5	0.10	0.0524	1.0648	156.5	456.5
		15		0.1264			
		35		0.2430			
		60		0.3871			
		90		> 0.5336			
UBA-1	0.9951	15	0.10	-	1.0648	156.5	456.5
UBA-2	0.9951	35	0.10	-	1.0648	156.5	456.5
UBA-3	0.9951	60	0.10	-	1.0648	156.5	456.5

5.3 The wind load

The structure-BA system is simulated under four wind flows of increasing intensity, lasting 10 minutes each and blowing in the *x* direction. For each intensity, deterministic wind load time-histories are applied to each structural node, computed as the realization of a stationary nonhomogeneous stochastic process, comprising both along-wind and across-wind fluctuating force components, so as to simultaneously excite the tower in the two directions. For each horizontal component, the wind force time-history at node *i* is computed as follows [47]:

$$F_i(t) = \sum_{j=1}^{i}\sum_{k=1}^{N_s}\left|\Gamma_{ij}(\omega_k^*)\right|\sqrt{2\Delta\omega_k^*}\cos(\omega_k^* t + \varphi_{jk}) \,, \qquad i = 1, 2, \ldots, N \tag{43}$$

where $N = 12$ is the total number of nodes; $N_s = 2^{14}$ is the total number of frequency intervals; $\Delta\omega_k^* = 0.01$ rad/s is the frequency interval; $\omega_k^* = (k-1)\Delta\omega_k^*$ is the generic input frequency; φ_{jk} is the phase angle, randomly distributed between 0 and 2π; and $\mathbf{\Gamma}(\omega_k^*)$ is the lower triangular matrix obtained through the Cholesky's factorization of the corresponding stochastic cross-spectrum matrix $\mathbf{S}_{FF}(\omega_k^*)$, on its turn expressed by Davenport's spectrum for the along-wind component [48], and by Vickery and Clarke's spectrum for the across-wind component [49]. In this study, the along-wind and across-wind $\mathbf{S}_{FF}(\omega_k^*)$ matrices are defined according to Eqs. (38) to (41) of ref. [40], and computed based on the following values of the relevant aerodynamic parameters: $\rho_a = 1.23$ kg/m^3; $\alpha = 0.25$; $C_d = 1.2$; $C_l = 7.0$; $K_0 = 0.01$; $C_l = 0.20$; $S = 0.12$; $B_s = 0.26$; $\alpha_1 = 0.5$; $\alpha_2 = 5.0$. Additionally, the reference mean wind velocity at 10 m above the ground, $\bar{V}_{10}$, is taken as, respectively, 15, 20, 25, and 30 m/s, for the four considered wind load intensities.

5.4 Results and discussion

Results are reported in Tables 7 to 10, for the four wind intensities. In each table, 8 cases are compared, corresponding to the uncontrolled structure and to the 7 controlled configurations. For each case, the following response quantities are reported as a measure of the absorber performance, expressed in both maximum and rms terms: u_s, v_s and r_s, respectively denoting the *x* (along-wind) component, the *y* (across-wind) component, and the overall (modulus) tower top displacement; $\ddot{u}_s$, $\ddot{v}_s$ and $\ddot{r}_s$, respectively denoting the *x* and *y* components and the overall (modulus) tower top acceleration; and *r*, denoting the overall (modulus) relative ball displacement.

Table 7. Maximum and rms responses for $\bar{V}_{10}$ = 15 m/s – Comparison of the uncontrolled and controlled cases.

Case	$u_{s\max}$ (mm)	$u_{s\,rms}$ (mm)	$v_{s\max}$ (mm)	$v_{s\,rms}$ (mm)	$r_{s\max}$ (mm)	$r_{s\,rms}$ (mm)	$\ddot{u}_{s\max}$ (m/s^2)	$\ddot{u}_{s\,rms}$ (m/s^2)	$\ddot{v}_{s\max}$ (m/s^2)	$\ddot{v}_{s\,rms}$ (m/s^2)	$\ddot{r}_{s\max}$ (m/s^2)	$\ddot{r}_{s\,rms}$ (m/s^2)	$r_{\max}$ (mm)	r_{rms} (mm)

Unc.	7.97	2.33	2.14	0.67	8.04	2.43	0.301	0.093	0.018	0.006	0.301	0.093	-	-
LBA	6.10	1.67	2.15	0.68	6.10	1.81	0.222	0.058	0.018	0.006	0.222	0.058	16.04	4.94
VBA	6.10	1.67	2.15	0.68	6.10	1.81	0.222	0.058	0.018	0.006	0.222	0.058	16.00	4.94
HBA	6.11	1.67	2.15	0.68	6.12	1.80	0.224	0.058	0.018	0.006	0.224	0.058	16.27	4.98
DBA	5.85	1.74	2.15	0.68	5.86	1.86	0.234	0.061	0.017	0.006	0.234	0.061	17.09	4.32
UBA-1	7.48	2.23	2.15	0.68	7.48	2.33	0.275	0.087	0.018	0.006	0.275	0.087	9.22	0.80
UBA-2	7.83	2.34	2.15	0.68	7.85	2.43	0.297	0.092	0.018	0.006	0.297	0.092	0.02	0.00
UBA-3	7.83	2.34	2.15	0.68	7.86	2.43	0.298	0.092	0.018	0.006	0.298	0.092	0.01	0.00

Table 8. Maximum and rms responses for $\overline{V}_{10}$ = 20 m/s – Comparison of the uncontrolled and controlled cases.

Case	$u_{s\max}$ (mm)	$u_{s\,rms}$ (mm)	$v_{s\max}$ (mm)	$v_{s\,rms}$ (mm)	$r_{s\max}$ (mm)	$r_{s\,rms}$ (mm)	$\ddot{u}_{s\max}$ (m/s^2)	$\ddot{u}_{s\,rms}$ (m/s^2)	$\ddot{v}_{s\max}$ (m/s^2)	$\ddot{v}_{s\,rms}$ (m/s^2)	$\ddot{r}_{s\max}$ (m/s^2)	$\ddot{r}_{s\,rms}$ (m/s^2)	$r_{\max}$ (mm)	r_{rms} (mm)
Unc.	16.9	4.8	5.4	1.6	16.9	5.0	0.732	0.201	0.110	0.029	0.732	0.203	-	-
LBA	10.3	3.1	5.7	1.6	10.4	3.5	0.455	0.116	0.117	0.028	0.458	0.120	35.5	10.2
VBA	10.3	3.1	5.7	1.6	10.4	3.5	0.454	0.117	0.117	0.028	0.457	0.120	35.1	10.2
HBA	10.3	3.1	5.5	1.6	10.3	3.5	0.455	0.116	0.109	0.028	0.457	0.120	35.0	10.2
DBA	10.2	3.1	5.5	1.6	10.4	3.5	0.457	0.117	0.109	0.028	0.460	0.120	35.0	10.0
UBA-1	11.7	3.5	5.5	1.6	11.7	3.9	0.497	0.139	0.111	0.029	0.497	0.142	49.3	8.5
UBA-2	17.1	4.6	5.4	1.6	17.2	4.9	0.743	0.192	0.107	0.030	0.743	0.194	34.1	3.2
UBA-3	19.1	5.0	5.4	1.6	19.1	5.3	0.838	0.210	0.107	0.030	0.838	0.212	3.0	0.1

Table 9. Maximum and rms responses for $\overline{V}_{10}$ = 25 m/s – Comparison of the uncontrolled and controlled cases.

Case	$u_{s\max}$ (mm)	$u_{s\,rms}$ (mm)	$v_{s\max}$ (mm)	$v_{s\,rms}$ (mm)	$r_{s\max}$ (mm)	$r_{s\,rms}$ (mm)	$\ddot{u}_{s\max}$ (m/s^2)	$\ddot{u}_{s\,rms}$ (m/s^2)	$\ddot{v}_{s\max}$ (m/s^2)	$\ddot{v}_{s\,rms}$ (m/s^2)	$\ddot{r}_{s\max}$ (m/s^2)	$\ddot{r}_{s\,rms}$ (m/s^2)	$r_{\max}$ (mm)	r_{rms} (mm)
Unc.	26.4	7.0	25.4	6.7	28.5	9.7	1.07	0.29	0.96	0.27	1.12	0.39	-	-
LBA	18.3	5.1	17.5	4.9	19.5	7.1	0.82	0.19	0.54	0.17	0.83	0.26	57.8	23.6
VBA	18.3	5.1	17.6	4.9	19.7	7.1	0.82	0.19	0.55	0.17	0.82	0.26	58.8	23.4
HBA	18.6	5.2	18.5	5.1	20.2	7.3	0.77	0.20	0.58	0.18	0.77	0.27	59.6	21.7
DBA	18.6	5.2	18.4	5.1	20.1	7.3	0.77	0.19	0.58	0.18	0.78	0.26	60.2	21.8
UBA-1	18.9	5.3	17.8	5.3	19.6	7.5	0.86	0.20	0.64	0.19	0.86	0.28	108.4	32.8
UBA-2	24.5	6.0	21.7	5.8	24.5	8.3	0.94	0.23	0.72	0.22	0.94	0.32	60.6	13.4
UBA-3	27.3	7.0	24.8	6.8	28.5	9.7	1.03	0.28	0.94	0.27	1.04	0.39	38.1	2.8

Table 10. Maximum and rms responses for $\overline{V}_{10}$ = 30 m/s – Comparison of the uncontrolled and controlled cases.

Case	$u_{s\max}$ (mm)	$u_{s\,rms}$ (mm)	$v_{s\max}$ (mm)	$v_{s\,rms}$ (mm)	$r_{s\max}$ (mm)	$r_{s\,rms}$ (mm)	$\ddot{u}_{s\max}$ (m/s^2)	$\ddot{u}_{s\,rms}$ (m/s^2)	$\ddot{v}_{s\max}$ (m/s^2)	$\ddot{v}_{s\,rms}$ (m/s^2)	$\ddot{r}_{s\max}$ (m/s^2)	$\ddot{r}_{s\,rms}$ (m/s^2)	$r_{\max}$ (mm)	r_{rms} (mm)
Unc.	38.2	11.0	78.3	20.2	81.5	23.0	1.60	0.47	3.34	0.88	3.45	1.00	-	-
LBA	28.7	7.4	42.2	11.3	42.2	13.5	1.16	0.29	1.72	0.46	1.73	0.55	178	54.1
VBA	30.7	7.7	44.3	11.9	44.5	14.2	1.29	0.31	1.86	0.49	1.89	0.58	141	52.0
HBA	30.3	7.8	42.7	11.9	45.6	14.2	1.16	0.31	1.77	0.49	1.85	0.58	133	48.8
DBA	30.7	7.7	42.7	11.9	44.8	14.2	1.20	0.31	1.76	0.49	1.85	0.58	144	49.7
UBA-1	43.9	11.4	49.9	14.0	53.5	18.0	1.80	0.48	2.11	0.59	2.37	0.76	156	84.8
UBA-2	42.4	8.9	46.1	12.7	52.1	15.5	1.98	0.37	1.98	0.53	2.21	0.64	156	62.8
UBA-3	33.7	8.6	49.1	13.3	49.1	15.9	1.37	0.35	2.07	0.56	2.09	0.66	153	42.4

Tables 7 to 10 above are summarized in Table 11, where the average overall response ratios, R_{av}, are reported for the 7 controlled cases and for each wind intensity, computed dividing the controlled to the

uncontrolled overall tower top response, and then geometrically averaging between displacements and accelerations, and between maximum and rms values. Obviously, R_{av} = 1 for the uncontrolled case, and the smaller R_{av}, the better the control effectiveness.

Table 11. Average overall response ratios, R_{av}, for the 7 controlled cases.

Case	$\overline{V}_{10}$ = 10 m/s	$\overline{V}_{10}$ = 20 m/s	$\overline{V}_{10}$ = 25 m/s	$\overline{V}_{10}$ = 30 m/s
LBA	0.71	0.63	0.70	0.54
VBA	0.71	0.63	0.70	0.57
HBA	0.71	0.63	0.71	0.57
DBA	0.73	0.63	0.71	0.57
UBA-1	0.93	0.71	0.73	0.72
UBA-2	0.99	0.99	0.84	0.65
UBA-3	0.99	1.09	0.98	0.64

Figure 16 shows the Fourier spectra of u_s and v_s when $\overline{V}_{10}$ = 25 m/s, respectively in the uncontrolled, the DBA-controlled and the UBA-2 controlled cases. Both the along-wind (Figure 16a) and the across-wind forces (Figure 16b) induce significant structural vibrations at low frequencies, i.e. outside the effective bandwidth of the absorbers. This explains the limited control efficacy of all BAs in this case study, if compared with their harmonic steady-state performance highlighted in previous sections. In the *y* direction, this effect is even more evident for $\overline{V}_{10}$ = 15 m/s or $\overline{V}_{10}$ = 20 m/s, when the wind action is substantially uncoupled from the first modal resonance (the vortex shedding frequencies being much lower than the first structural frequency), and all BAs are practically ineffective.

With this in mind, Tables 7 to 11 can be commented as follows:

1) In the uncontrolled case, the structural response is dominated by the along-wind component for $\overline{V}_{10}$ = 15÷20 m/s and by the across-wind component for $\overline{V}_{10}$ = 30 m/s, while it is equally contributed by both components for $\overline{V}_{10}$ = 25 m/s. As $\overline{V}_{10}$ increases from 15 m/s to 30 m/s, the overall structural displacements and accelerations, r_s and $\ddot{r}_s$, increase about 10 times, both in maximum and rms terms.
2) The LBA, representative of an ideal linear absorber, is quite effective, considering the limited coupling between the structure and the wind load, and the very small value of the mass ratio. The response is reduced to R_{av} = 63÷71% for $\overline{V}_{10}$ = 15÷25 m/s, and to R_{av} = 54% for $\overline{V}_{10}$ = 30 m/s, with the device slightly more effective in controlling accelerations than displacements. Depending on $\overline{V}_{10}$, significant differences exist between the along-wind and the across-wind performance, according to the wind load frequency content: for $\overline{V}_{10}$ = 15÷20 m/s, the device reduces the along-wind average response to 66%, but cannot reduce the across-wind vibrations; for $\overline{V}_{10}$ = 25 m/s, it reduces the two components to, respectively, 71% and 66%; and for $\overline{V}_{10}$ = 30 m/s it reduces them to, respectively, 69% and 53%. Depending on $\overline{V}_{10}$, the maximum and the rms ball displacements, r_{max} and r_{rms}, range, respectively, from 16 mm to 178 mm (this latter value being larger than the VBA virtual radius *L*, in fact equal to 159.2 mm, see Table 5) and from 5 mm to 54 mm.
3) The VBA, the HBA and the DBA show approximately the same performance as the LBA, except for a small control loss for $\overline{V}_{10}$ = 30 m/s, when R_{av} increases from 54% to 57%. This loss is due to second-order effects caused by the large angular displacements exhibited by the ball at this excitation level (with r_{max} around 90% of *L*). Evidently, for $\overline{V}_{10} \geq$ 30 m/s, a first-order model is no longer adequate.

4) The three UBA options, instead, show severe performance losses with respect to the LBA, varying for each option with the wind intensity. For $\overline{V}_{10}$ = 15 m/s, the UBA-2 and the UBA-3 are virtually inactive, because of their excessive friction, while the UBA-1 is only partially activated and clearly overdamped, exhibiting small ball displacements and a limited control effectiveness (R_{av} = 93%). For $\overline{V}_{10}$ = 20 m/s, the UBA-3 is still inactive (and even detrimental, with R_{av} = 109%) and the UBA-2 starts being activated but is still largely overdamped (R_{av} = 99%), while the UBA-1 is fully activated and yet less effective than its viscous or homogeneous counterparts (R_{av} = 71% instead of R_{av} = 63%), because in fact respectively overdamped or underdamped according if the ball displacements are small or large. For $\overline{V}_{10}$ = 25 m/s, the UBA-1, UBA-2 and UBA-3 are respectively slightly underdamped, slightly overdamped, and largely overdamped, with respectively R_{av} = 73%, 84%, and 98% (instead of R_{av} = 70÷71% for the other types). Finally, for $\overline{V}_{10}$ = 30 m/s, the UBA-1 and UBA-2 are respectively largely underdamped and slightly underdamped, while the UBA-3 is overdamped at small ball displacements and underdamper at large ball displacements, with respectively R_{av} = 72%, 65%, and 64% (instead of R_{av} = 54% for the LBA and R_{av} = 57% for the other types). Part of this control loss may be due to second-order effects, due to the large ball displacements exhibited at this excitation level (with $r_{\max}$ close to 100% of L).

In conclusion, this case study shows the adequacy of the HBA and of the DBA to replicate the control effectiveness of the VBA, and their advantages over a conventional, constant friction, UBA, whose performance can be nearly optimal only at a certain vibration amplitude. Furthermore, it shows the need of using a fully nonlinear model to account for the possible control loss related to second-order effects.

6. Conclusions

The main conclusions of this paper can be summarized as follows:

1) The ball absorber (BA) is a simple, compact and low-cost vibration control device, only slightly less effective, because of its rotational inertia, than a point-mass pendulum absorber.
2) The conventional, uniform BA (UBA), having a constant friction along the cavity, shows an amplitude-dependent control performance, its equivalent damping being inversely proportional to the input amplitude as far as its response is confined into the low-amplitude domain.
3) The new, homogeneous BA (HBA), having a friction that varies along the cavity in proportion to the ball angular displacement, shows a performance that is amplitude independent in the low-amplitude domain, its equivalent damping being constant with the input amplitude. In the large-amplitude domain, the friction increase is advantageously more gradual than in similar solutions recently proposed for point-mass pendulum absorbers.
4) The new, discrete-homogeneous BA (DBA), obtained by juxtaposing n coating regions with radially-increasing friction so as to approximate the HBA friction linear variation, degenerates in the UBA if n = 1, and in the HBA if n tends to infinity, showing a nearly amplitude-independent control performance if n is sufficiently large.
5) The proposed fully nonlinear analytical model can adequately simulate viscous BAs (VBAs), UBAs, HBAs and DBAs on generic linear structures. A special variant of the friction model, incorporating a velocity-dependent transition law, is also formulated, that better fits experimental tests.
6) The first-order approximation of the model, rigorously valid in the low-amplitude domain, reveals the main features of the four BA types, and permits the development of an optimal design procedure.
7) For the VBA, UBA and HBA, the optimal procedure consists in an H_∞ design. The optimal solution is amplitude independent for the VBA and the HBA, but amplitude dependent for the UBA, its optimal friction being amplitude-proportional. While the optimal VBA and HBA are nearly equivalent, the UBA underperforms them if the input amplitude differs from that assumed

in design. Fitting many optimal solutions, practical design formulas are derived for the VBA, approximately valid for the HBA as well.

8) For the DBA, the optimal design procedure consists in finding the DBA that best fits the optimal HBA, for a given *n*. The optimization problem can be formulated either directly or inversely, depending on which DBA parameters are chosen as the design variables, and can be solved analytically for $n = 1$ and numerically otherwise.
9) The feasibility of the DBA concept, the validity of the analytical model and the effectiveness of the design procedure are demonstrated through building and testing a scaled prototype of DBA, in comparison with a similar prototype of UBA. The DBA proves more efficient and robust than the UBA.
10) The simulated design of different BAs for the wind control of an airport tower shows the adequacy of the HBA and of the DBA to replicate the effectiveness of an optimal VBA, and their superiority over a conventional UBA, whose performance is highly affected by the vibration level.

Acknowledgements
This research was kindly supported by Politecnico di Torino. Special thanks go to Prof. Donato Sabia and Dr. Antonino Quattrone in MastrLab, for supporting equipment.

Appendix A. Practical design formulas for determining the H_∞ optimal parameters of a VBA

This appendix provides practical design formulas for determining the H_∞ optimal parameters ω_{Ropt} and ζ_{opt} of a VBA as a function of the structural damping ratio ζ_{sx}, the mass ratio m_R and the inertia coefficient κ. These formulas are derived by fitting, through a least-square minimization, the values of ω_{Ropt} and ζ_{opt} obtained by numerically solving the min.max problem in Eq. (34) for all the possible combinations of $\zeta_{sx} = [1, 2, 5]/100$, $m_R = [0.1:0.1:0.9, 1:0.2:1.8, 2:1:9, 10:5:100]/100$ and $\kappa = [0:0.1:1, 2/3]$ (with a total of 3·41·12 = 1476 design scenarios). Two cases are considered in the sequel, according as the transfer function $TF(\omega^*)$ is chosen as the force-to-displacement TF or as the ground acceleration-to-displacement TF.

A.1 Force input

For a VBA satisfying Eqs. (27) and (30), the modulus of the normalized TF from the force input $\bar{f}_{sx}$ to the structural displacement u_s is given by

$$|TF| = \left| \frac{2\zeta_{sx}\sqrt{1-\zeta_{sx}^2}}{1 + i2\zeta_{sx}\overline{\omega} - \overline{\omega}^2(1+m_R\Gamma)} \right| \tag{A.1}$$

where $\overline{\omega} = \omega^* / \omega_{sx}$ and

$$\Gamma = 1 + \frac{\overline{\omega}^2}{(1+\kappa)\left(\omega_R^2 + i2\zeta_{2x}\omega_R\overline{\omega} - \overline{\omega}^2\right)} \tag{A.2}$$

Thus, the numerical solution of Eq. (34), repeated for the said combinations of ζ_{sx}, m_R and κ, provides the optimal values of ω_{Ropt} and ζ_{opt}, whose dependence on ζ_{sx}, m_R and κ can be conveniently approximated by the following expressions:

$$\omega_{Ropt} = A_1(m_R)A_2(m_R, \zeta_{sx})A_3(m_R, \zeta_{sx}, \kappa) \tag{A.3}$$

$$\zeta_{opt} = [A_4(m_R) + A_5(m_R, \zeta_{sx})]A_6(m_R, \kappa) \tag{A.4}$$

where the functions A_i are defined as

$$A_1(m_R)=\frac{1}{1+m_R} \qquad A_2(m_R,\zeta_{sx})=\frac{1}{1+p_1 m_R^{p2}\zeta_{sx}} \qquad A_3(m_R,\zeta_{sx},\kappa)=1+m_R^{p3}(p_4+p_5\zeta_{sx})\kappa^{p_6} \tag{A.5}$$

$$A_4(m_R)=\sqrt{\frac{3m_R}{8(1+m_R)}} \qquad A_5(m_R,\zeta_{sx})=p_7 m_R\zeta_{sx}^{p_8}+p_9\zeta_{sx} \qquad A_6(m_R,\kappa)=1-(p_{10}+p_{11}m_R^{p12})\kappa^{p_{13}} \tag{A.6}$$

and their fitting coefficients p_1 to p_{13} are given in Table A.1.

Noticeably, for $\zeta_{sx}=\kappa=0$ Eqs. (A.3) and (A.4) reduce to, respectively, $\omega_{Ropt}=A_1(m_R)=1/(1+m_R)$ and $\zeta_{opt}=A_4(m_R)=\sqrt{3m_R/[8(1+m_R)]}$, i.e. to the classical Warburton's formulae [1], indeed exact for an undamped structure and a null ball rotational inertia.

For example, the optimal parameters and their corresponding response ratios are reported in Figure A.1 as a function of m_R, for $\zeta_{sx}=2\%$ and for different values of κ. The dots indicate the numerical optima while the continuous lines indicate their fitting expressions in Eqs. (A.3) and (A.4).

Table A.1. VBA design for a force input. Optimal fitting coefficients in Eqs. (A.5) and (A.6).

p_1	p_2	p_3	p_4	p_5	p_6	p_7	p_8	p_9	p_{10}	p_{11}	p_{12}	p_{13}
1.1527	.3881	.9325	.2332	.6505	0.6344	.01242	.0001	.1351	.2304	.08020	.09793	0.7265

A.2 Ground acceleration input

For a VBA satisfying Eqs. (27) and (30), the modulus of the normalized transfer function from the ground acceleration input $\ddot{u}_g$ to the structural displacement u_s is given by

$$|TF|=\left|\frac{2\zeta_{sx}\sqrt{1-\zeta_{sx}^2}\,(1+m_R\Gamma)}{1+i2\zeta_{sx}\overline{\omega}-\overline{\omega}^2(1+m_R\Gamma)}\right| \tag{A.7}$$

where Γ is still given by Eq. (A.2). In this case, the numerical solution of Eq. (34) can be approximated by

$$\omega_{Ropt}=B_1(m_R)B_2(m_R,\zeta_{sx})B_3(m_R,\zeta_{sx},\kappa) \tag{A.8}$$

$$\zeta_{opt}=[B_4(m_R)+B_5(m_R,\zeta_{sx})]B_6(m_R,\zeta_{sx},\kappa) \tag{A.9}$$

where the functions B_i are defined as

$$B_1(m_R)=\frac{\sqrt{1-m_R/2}}{1+m_R} \qquad B_2(m_R,\zeta_{sx})=\frac{1}{1+(\sqrt{m_R}+q_1 m_R^3)(q_2\zeta_{sx}^{q_3}+q_4\zeta_{sx}+q_5\zeta_{sx}^2)} \tag{A.10}$$

$$B_3(m_R,\zeta_{sx},\kappa)=1+(m_R+q_6 m_R^{q_7})(q_8+q_9\zeta_{sx})\kappa^{q_{10}}$$

$$B_4(m_R)=\sqrt{\frac{3m_R}{8(1+m_R)(1-m_R/2)}} \qquad B_5(m_R,\zeta_{sx})=m_R^{q_{11}}(-q_{12}\zeta_{sx}^{q_{13}}+q_{14}\zeta_{sx})+q_{15}\zeta_{sx} \tag{A.11}$$

$$B_6(m_R,\zeta_{sx},\kappa)=1-\frac{m_R^{q_{16}}(q_{17}+q_{18}\zeta_{sx})\kappa}{(1+q_{19}\kappa)}-(q_{20}-q_{21}\zeta_{sx})\kappa^{q_{22}}$$

and their fitting coefficients q_1 to q_{22} are given in Table A.2.

Again, for $\zeta_{sx} = \kappa = 0$ Eqs. (A.8) and (A.9) reduce to, respectively, $\omega_{Ropt} = B_1(m_R) = \sqrt{1 - m_R/2}\,/(1 + m_R)$ and $\zeta_{opt} = B_4(m_R) = \sqrt{3m_R/[8(1+m_R)(1-m_R/2)]}$, i.e. to the classical Warburton's formulae [1]. Results are exemplified in Figure A.2 for $\zeta_{sx} = 2\%$ and for different values of κ.

Table A.2. VBA design for a ground acceleration input. Optimal fitting coefficients in Eqs. (A.10) and (A.11).

q_1	q_2	q_3	q_4	q_5	q_6	q_7	q_8	q_9	q_{10}	q_{11}
.6423	.002455	0.0001	2.0875	8.4404	.5979	3.071	.3958	2.363	.6050	2.1150

Table A.2. (continues)

q_{12}	q_{13}	q_{14}	q_{15}	q_{16}	q_{17}	q_{18}	q_{19}	q_{20}	q_{21}	q_{22}
.03170	.0001	1.239	.1422	1.253	.8145	6.620	4.522	.2939	.3850	0.7325

A.3 Discussion

Equations (A.3) and (A.4) for the force input case and (A.8) and (A.9) for the ground acceleration input case constitute useful design formulas for deriving the H_∞ optimal parameters of a VBA. They fit the numerical optima with a good accuracy. The average error (over all the examined 1476 design scenarios), respectively in terms of ω_{Ropt}, ζ_{opt}, and $R_{\infty opt}$, is equal to 1.2‰, 6.6‰, and 3.3‰ for the force input, and to 2.4‰, 7.5‰, and 5.2‰ for the ground acceleration input. The influence of the ball rotational inertia, expressed by κ, on the VBA optimal design parameters and control effectiveness is demonstrated in Figures A.1 and A.2. The derivation of similar expressions for friction-type BAs is left for future work.

References

1. G.B. Warburton, Optimum absorber parameters for various combinations of response and excitation parameters, Earth. Eng. Struct. Dyn. 10 (1982) 381–401.
2. K.C.S. Kwok, B. Samali, Performance of tuned mass dampers under wind loads, Eng. Struct. 17/9 (1995) 655–667.
3. N. Hoang, Y. Fujino, P. Warnitchai, Optimal tuned mass damper for seismic applications and practical design formulas, Eng. Struct. 30/3 (2008) 707–715.
4. K.K.F. Wong, Seismic energy dissipation of inelastic structures with tuned mass dampers, J. Eng. Mech. 134/2 (2008) 163–172.
5. A.A. Taflanidis, D.C. Angelides, J.T. Scruggs, Simulation-based robust design of mass dampers for response mitigation of tension leg platforms, Eng. Struct. 31 (2009) 847–857.
6. M.F. Huang, K.T. Tse, C.M. Chan, W.J. Lou, Integrated structural optimization and vibration control for improving wind-induced dynamic performance of tall buildings, Int. J. Struct. Stab. Dyn. 11/6 (2011) 1139–1161.
7. R. Greco, G.C. Marano, Optimum design of Tuned Mass Dampers by displacement, Soil Dyn. Earthq. Eng. 49 (2013) 243–253.
8. D. Wang, T.K.T. Tse, Y. Zhou, Q. Li, Structural performance and cost analysis of wind-induced vibration control schemes for a real super-tall building, Struct. Infrastruct. Eng. 11/8 (2015) 990–1011.
9. E. Matta, Seismic effectiveness of tuned mass dampers in a life-cycle cost perspective, Earthq. Struct. 9/1 (2015) 73–91.
10. R. Ruiz, A.A. Taflanidis, D. Lopez-Garcia, C.R. Vetter, Life-cycle based design of mass dampers for the Chilean region and its application for the evaluation of the effectiveness of tuned liquid dampers with floating roof, Bull. Earthq. Eng. 14 (2016) 943–970.
11. R. Greco, G.C. Marano, A. Fiore, Performance-cost optimization of tuned mass damper under low-moderate seismic actions, Struct. Des. Tall Spec. Build. 25/18 (2016) 1103–1122.

12. S. Elias, V. Matsagar, Research developments in vibration control of structures using passive tuned mass dampers, Annu Rev Control 44 (2017) 129–156.
13. E. Matta, Lifecycle cost optimization of tuned mass dampers for the seismic improvement of inelastic structures, Earthq. Eng. Struct. Dyn. 47 (2017) 714–737.
14. V.P. Legeza, Dynamics of vibroprotective systems with roller dampers of low-frequency vibrations, Strength Mat. 36/2 (2004) 185–194.
15. E. Matta, A. De Stefano, Seismic performance of pendulum and translational roof-garden TMDs, Mech. Syst. Signal Proc. 23 (2009) 908–921.
16. M. Bransch, Unbalanced oil filled sphere as rolling pendulum on a flat surface to damp horizontal structural vibrations, J. Sound Vibr. 368 (2016) 22–35.
17. X. Lu, Z. Liu, Z. Lu, Optimization design and experimental verification of track nonlinear energy sink for vibration control under seismic excitation, Struct. Control Health Monit. 24/12 (2017) e2033.
18. M. Pirner, Actual behaviour of a ball vibration absorber, J. Wind Eng. Ind. Aerodyn. 90 (2002) 987–1005.
19. E. Matta, A. De Stefano, B.F. Spencer Jr., A new passive rolling-pendulum vibration absorber using a non-axial-symmetrical guide to achieve bidirectional tuning, Earthq. Eng. Struct. Dyn. 38 (2009) 1729–1750.
20. J. Náprstek, C. Fischer, M. Pirner, O. Fischer, Non-linear model of a ball vibration absorber, Comput. Meth. Applied Sciences 30 (2013) 381–396.
21. M. Pirner, Dissipation of kinetic energy of large-span bridges, Acta Tech. CSAV 39 (1994) 645–655.
22. V. P. Legeza, Rolling of a heavy ball in a spherical recess of a translationally moving body, Int. Appl. Mech. 38/6 (2002) 758–764.
23. J. Naprstek, C. Fischer, Auto-parametric semi-trivial and post-critical response of a spherical pendulum damper, Comput. Struct. 87 (2009) 1204–1215.
24. V.P. Legeza, Dynamics of vibration isolation system with a ball vibration absorber, Int. Applied Mech. 54/5 (2018) 584–593.
25. J. Chen, C.T. Georgakis, Tuned rolling-ball dampers for vibration control in wind turbines, J. Sound Vibr. 332 (2013) 5271–5282.
26. Z.-L. Zhang, J.-B. Chen, J. Li, Theoretical study and experimental verification of vibration control of offshore wind turbines by a ball vibration absorber, Struct. Infrastr. Eng. 10/8 (2014) 1087–1100.
27. S. Li, L. Fu, F. Kong, Seismic response reduction of structures equipped with a voided biaxial slab-based tuned rolling mass damper, Shock and Vibration 2015/760394 (2015) 1–15.
28. P.S. Harvey Jr., K.C. Kelly, A review of rolling-type seismic isolation: historical development and future directions, Eng. Struct. 125 (2016) 521–531.
29. D. Foti, J.M. Kelly, Experimental analysis of a model isolated at the base with rubber-layer roller bearing (RLRB), Euro Earthq. Eng. 10/3 (1996) 3–13.
30. A.H. Muhr M. Sulong, A.G. Thomas, Rolling-ball rubber-layer isolators, J. Nat. Rubber Res. 12/4 (1997) 199–214.
31. L. Guerreiro, J. Azevedo, A.H. Muhr, Seismic tests and numerical modeling of a rolling-ball isolation system, J. Earthq. Eng. 11/1 (2007) 49–66.
32. J.W. Butterworth, Seismic response of a non-concentric rolling isolator system, Adv. Struct. Eng. 9/39 (2006) 39–53.
33. P.S. Harvey Jr., G.-P. Zéhil, H.P. Gavin, Experimental validation of simplified models for rolling isolation systems, Earthq. Eng. Struct. Dyn. 43 (2014) 1067–88.
34. B.-G. Jeon, S.-J. Chang, S.-W. Kim, N.-S. Kim, Base isolation performance of a conetype friction pendulum bearing system, Struct. Eng. Mech. 53 (2015) 227–48.
35. A. Fiore, G.C. Marano, M.N. Natale, Theoretical prediction of the dynamic behavior of rolling-ball rubber-layer isolation systems, Struct. Control Health. Monit. 23 (2016) 1150–1167.
36. F. Ricciardelli, B.J. Vickery, Tuned vibration absorbers with dry friction damping, Earthq. Eng. Struct. Dyn. 28/7 (1999) 707–723.

37. J. Inaudi, J. Kelly, Mass damper using friction-dissipating devices, J. Eng. Mech. 121 (1995) 142–149.
38. J.L. Almazan, J.C. De la Llera, J.A. Inaudi, D. Lopez-Garcia, L.E. Izquierdo, A Bidirectional and homogeneous tuned mass damper: a new device for passive control of vibrations, Eng. Struct. 29 (2007) 1548–1560.
39. E. Matta, A novel bidirectional pendulum tuned mass damper using variable homogeneous friction to achieve amplitude-independent control, Earth. Eng. Struct. Dyn (approved Jan. 2019, in press).
40. E. Matta, Modeling and design of bidirectional pendulum tuned mass dampers using axial or tangential homogeneous friction damping, Mech. Syst. Signal Proc. 116 (2019) 392–414.
41. A.D. Lewis, The geometry of the Gibbs-Appell equations and Gauss's principle of least constraint, Reports Math. Physics 38 (1996) 11-28.
42. J. Naprstek, C. Fischer, Non-holonomic dynamics of a ball moving inside a spherical cavity, Procedia Engineering 199 (2017) 613–618.
43. R. Greco, G.C. Marano, Identification of parameters of Maxwell and Kelvin-Voigt generalized models for fluid viscous dampers, J. Vibr. Control 21/2 (2015), 260–274.
44. MATLAB 2016b, The MathWorks, Inc., Natick, Massachusetts, United States.
45. K. Fujii, Y. Tamura, T. Sato, T. Wakahara, Wind-induced vibration of tower and practical applications of tuned sloshing damper, J. Wind Eng. And Industr. Aerodyn. 33 (1990) 263–272.
46. Y. Tamura, K. Fujii, T. Ohtsuki, T. Wakahara, R. Kohsaka, Effectiveness of tuned liquid damper under wind excitation, Eng. Structures 17/9 (1995) 609–621.
47. M. Shinozuka, G. Deodatis, Simulation of stochastic processes by spectral representation, J. Appl. Mech., 44/4 (1991) 191–204.
48. A.G. Davenport, The spectrum of horizontal gustiness near the ground in high winds, Q. J. R. Meteorol. Soc. 87 (1961) 194–211.
49. B.J. Vickery, A.W. Clarke, Lift or across-wind response of tapered stacks, J. Struct. Div. ASCE 98 (1972) 1–20.

List of Figures

Fig. 1. Typical pendulum vibration absorbers: (a to c) classical supported pendulums; (d) unbalanced pendulums [16]; (e) track NES [17]; (f) ball pendulum [18].

Fig. 2. Schematic *xz* meridian section of the ball absorber in its deformed position.

Fig. 3. Schematic planar view of the cavity coating with superimposed the corresponding friction law, in the case of: (a) uniform friction (UBA); (b) homogeneously varying friction (HBA); (c) discretely varying friction (DBA).

Fig. 4. Steady-state response of the first-order 2DOF model under a harmonic force input. Comparison of the VBA, the UBA and the HBA, for $\zeta_{sx} = 1\%$, $m_R = 1\%$ and either $\kappa = 0$ or $\kappa = 0.4$: (a) TFs for the three optimal BAs (for $\kappa = 0$ or $\kappa = 0.4$); (b) dissipative force-displacement loops for the three optimal BAs (for $\kappa = 0.4$); (c) TFs for the UBA, under increasing scaling factors of the input amplitude used for optimization (for $\kappa = 0.4$).

Fig. 5. Optimal design of a 1-step DBA by fitting an optimal HBA: (a) HBA and DBA friction laws $\mu(\theta)$; (b) HBA and DBA dissipated energies $\overline{E}(\theta)$.

Fig. 6. Optimal design of a 5-step DBA by fitting an optimal HBA, according to the direct approach: (a) HBA and DBA friction laws $\mu(\theta)$; (b) HBA and DBA dissipated energies $\overline{E}(\theta)$.

Fig. 7. Optimal design of a 3-step DBA by fitting an optimal HBA, according to the inverse approach: (a) HBA and DBA friction laws $\mu(\theta)$; (b) HBA and DBA dissipated energies $\overline{E}(\theta)$. Results refer to the optimal design of the DBA prototype detailed in Section 4.

Fig. 8. The overall experimental setup: (a) photo; (b) schematic drawing.

Fig. 9. Free acceleration response at the top of the uncontrolled structure along *x*, measured by S_2: (a) time response; (b) Fourier transform; (c) spectrogram; (d) instantaneous equivalent damping ratio as a function of the acceleration amplitude.

Fig. 10. Free-vibration tests of the UBA prototype with material 2 and ball radius $R = 10$ mm: (a) photo of the tested cap; (b) image acquisition and processing of the video recordings, for six consecutive frames (dimensions in pixels); (c) reconstruction of the experimental ball displacement time-history (dimensions in mm).

Fig. 11. Experimental and simulated ball displacement time-histories for the four UBAs, with $R = 10$ mm.

Fig. 12. (a) Photo of the UBA and DBA prototypes later tested on the tubular structure. (b) experimental and simulated ball displacement time-history for the fixed-base DBA. Added in dotted line: the simulated response of the ideal optimal HBA.

Fig. 13. Experimental free-vibration testing of the structure coupled with either the UBA or the DBA prototypes: (a) top structural accelerations measured by S_2; (b) corresponding instantaneous acceleration amplitudes; (c) instantaneous equivalent viscous damping ratio as a function of the acceleration amplitude. Black lines: 11 UBA tests where the absorber gets activated. Green lines: 10 UBA tests where the absorber remains inactive. Red lines: 21 DBA tests.

Fig. 14. Experimental shaking-table testing of the structure, with or without the UBA or DBA prototypes. Numbers in the legend denote the rms of each base acceleration time-history, in cm/s^2.

Fig. 15. Comparison of the HBA, the DBA, and the three UBA options, as characterized by Tables 5 and 6: (a) friction laws $\mu(\theta)$; (b) dissipated energies $\bar{E}(\theta)$.

Fig. 16. Fourier spectra of the top displacement in the *x* (a) and *y* (b) directions when $\overline{V}_{10}$ = 25 m/s, for the uncontrolled, the DBA controlled and the UBA-2 controlled cases.

Fig. A.1. VBA design for a force input. Optimal VBA parameters ω_{Ropt} (left) and ζ_{opt} (middle), and their corresponding response ratio $R_{\infty opt}$ (right) as a function of m_R, for $\zeta_{sx} = 2\%$ and for different values of κ (κ = 0: point mass; κ = 2/5: homogeneous sphere; κ = 2/3: hollow sphere; κ = 1: hollow cylinder). Dots: numerical optima; continuous lines: fitting curves.

Fig. A.2. VBA design for a ground acceleration input. Optimal VBA parameters ω_{Ropt} (left) and ζ_{opt} (middle), and their corresponding response ratio $R_{\infty opt}$ (right) as a function of m_R, for $\zeta_{sx} = 2\%$ and for different values of κ (κ = 0: point mass; κ = 2/5: homogeneous sphere; κ = 2/3: hollow sphere; κ = 1: hollow cylinder). Dots: numerical optima; continuous lines: fitting curves.

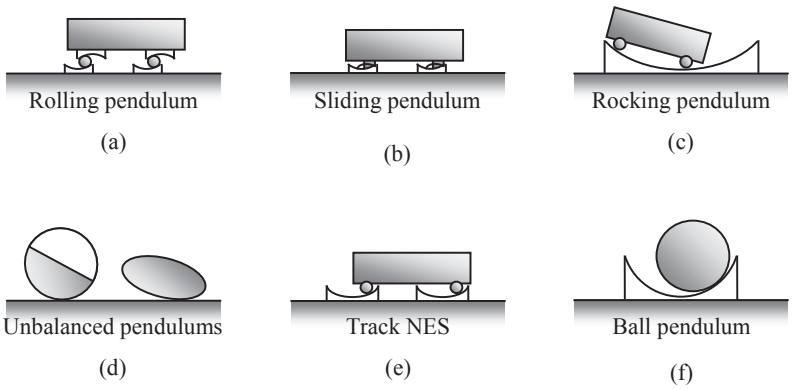
Rolling pendulum
(a)
Sliding pendulum
(b)
Rocking pendulum
(c)
Unbalanced pendulums
(d)
Track NES
(e)
Ball pendulum
(f)

Fig. 1.

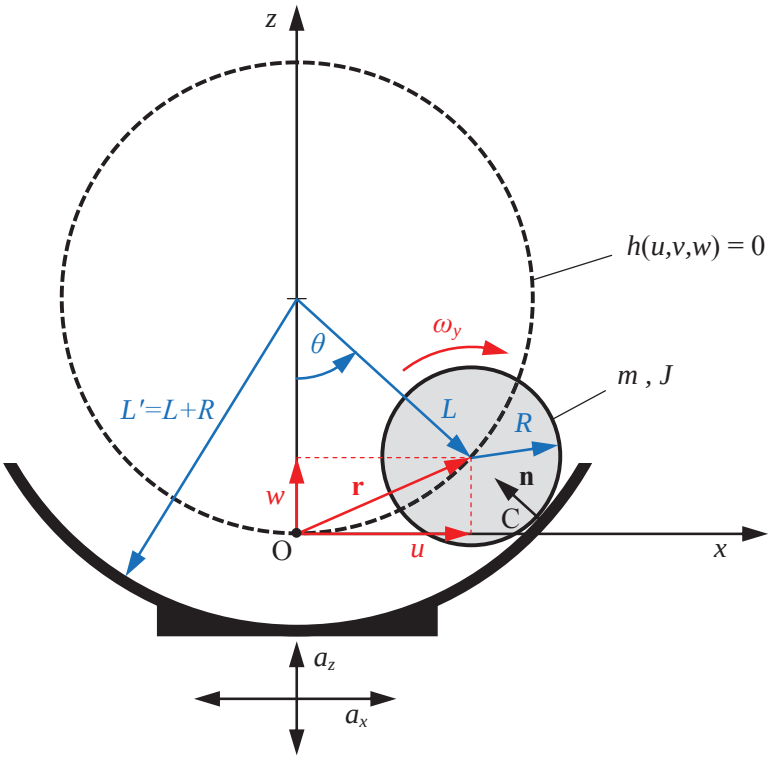

Fig. 2.

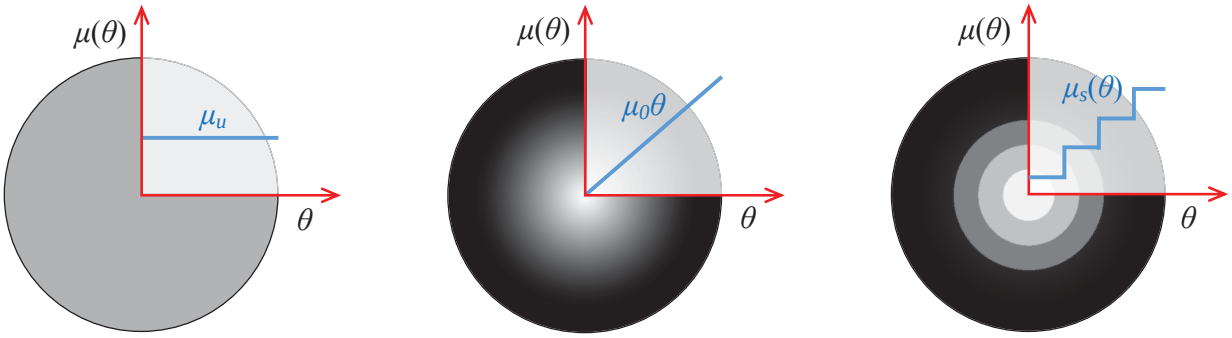

Fig. 3.

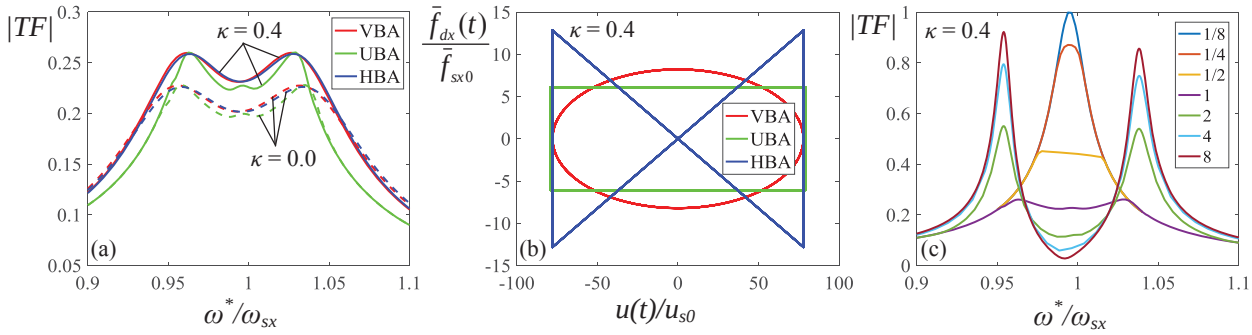
|TF|
κ = 0.4
κ = 0.0
VBA
UBA
HBA
(a)
ω*/ωsx
f̄dx(t)/f̄sx0
κ = 0.4
VBA
UBA
HBA
(b)
u(t)/us0
|TF|
κ = 0.4
1/8
1/4
1/2
1
2
4
8
(c)
ω*/ωsx

Fig. 4.

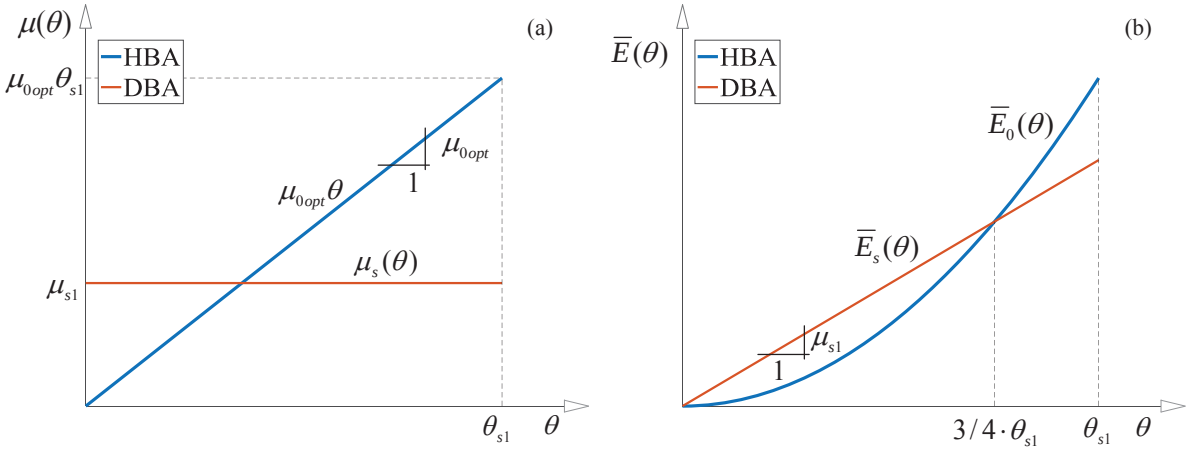
μ(θ)
(a)
HBA
DBA
μ0optθs1
μ0opt
1
μ0optθ
μs(θ)
μs1
θs1
θ
E(θ)
(b)
HBA
DBA
E0(θ)
Es(θ)
μs1
1
3/4·θs1
θs1
θ

Fig. 5.

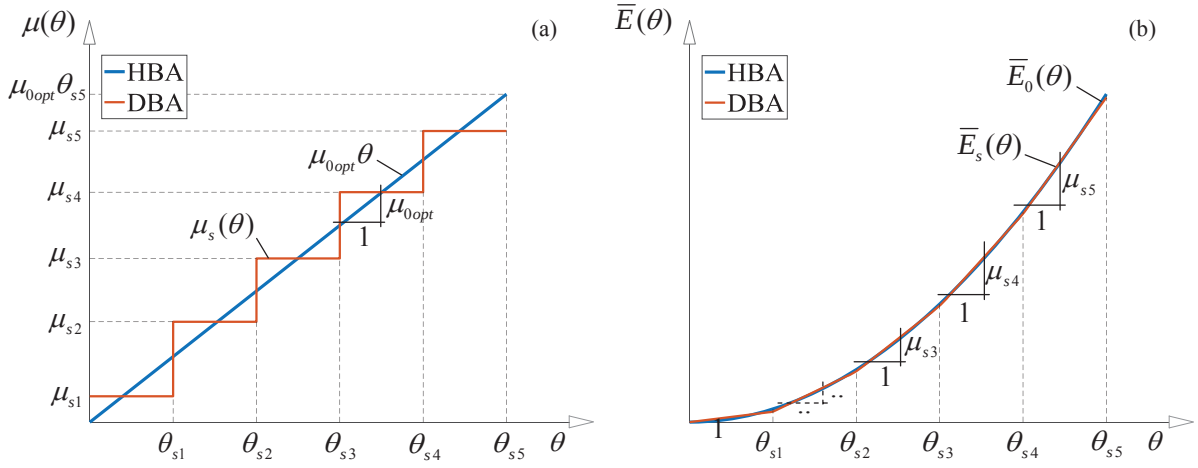
$\mu(\theta)$
(a)
HBA
DBA
$\mu_{0opt}\theta_{s5}$
μ_{s5}
μ_{s4}
μ_{s3}
μ_{s2}
μ_{s1}
$\mu_{0opt}\theta$
μ_{0opt}
$\mu_s(\theta)$
1
θ_{s1}
θ_{s2}
θ_{s3}
θ_{s4}
θ_{s5}
θ
$\overline{E}(\theta)$
(b)
HBA
DBA
$\overline{E}_0(\theta)$
$\overline{E}_s(\theta)$
μ_{s5}
μ_{s4}
μ_{s3}
1
θ_{s1}
θ_{s2}
θ_{s3}
θ_{s4}
θ_{s5}
θ

Fig. 6.

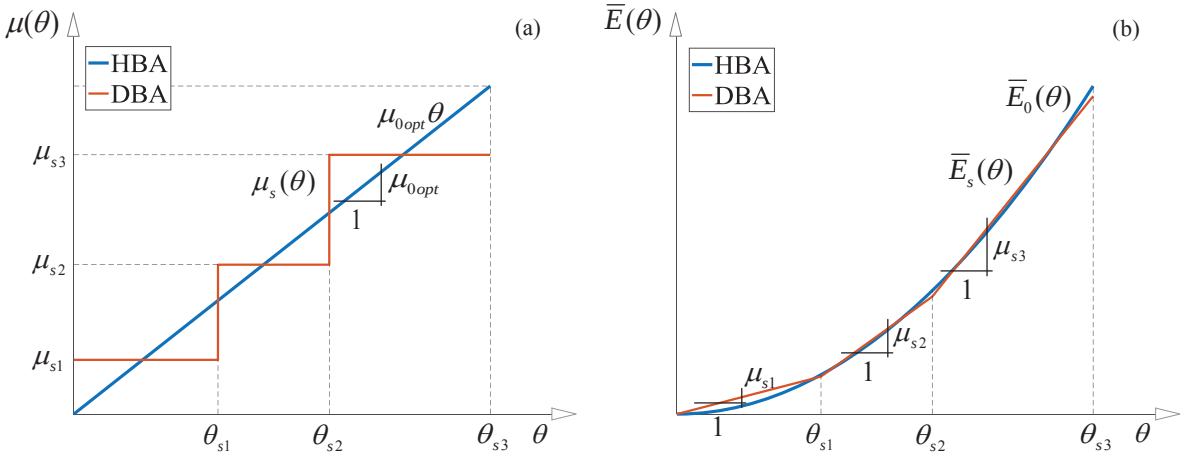
$\mu(\theta)$
(a)
HBA
DBA
$\mu_{0opt}\theta$
μ_{s3}
$\mu_s(\theta)$
μ_{0opt}
1
μ_{s2}
μ_{s1}
θ_{s1}
θ_{s2}
θ_{s3}
θ
$\overline{E}(\theta)$
(b)
HBA
DBA
$\overline{E}_0(\theta)$
$\overline{E}_s(\theta)$
μ_{s3}
1
μ_{s2}
1
μ_{s1}
1
θ_{s1}
θ_{s2}
θ_{s3}
θ

Fig. 7.

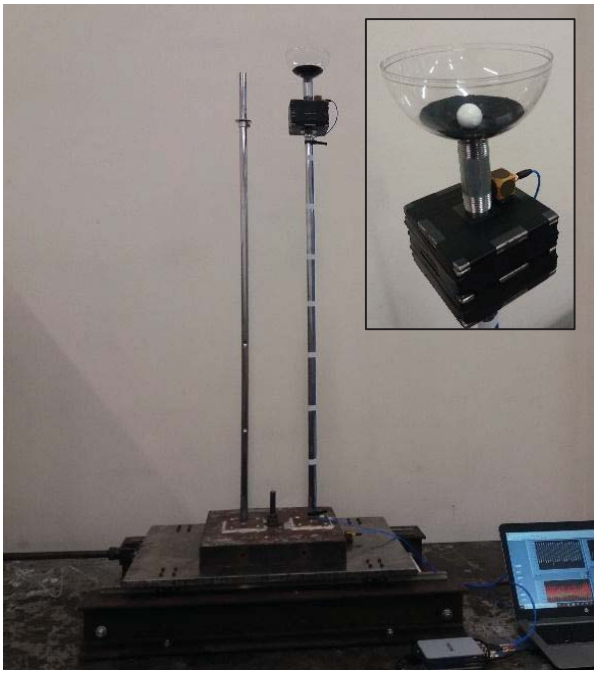

(a)

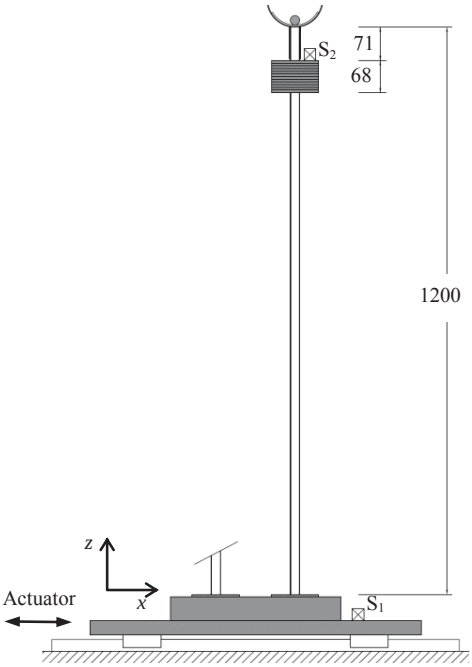

(b)

Fig. 8.

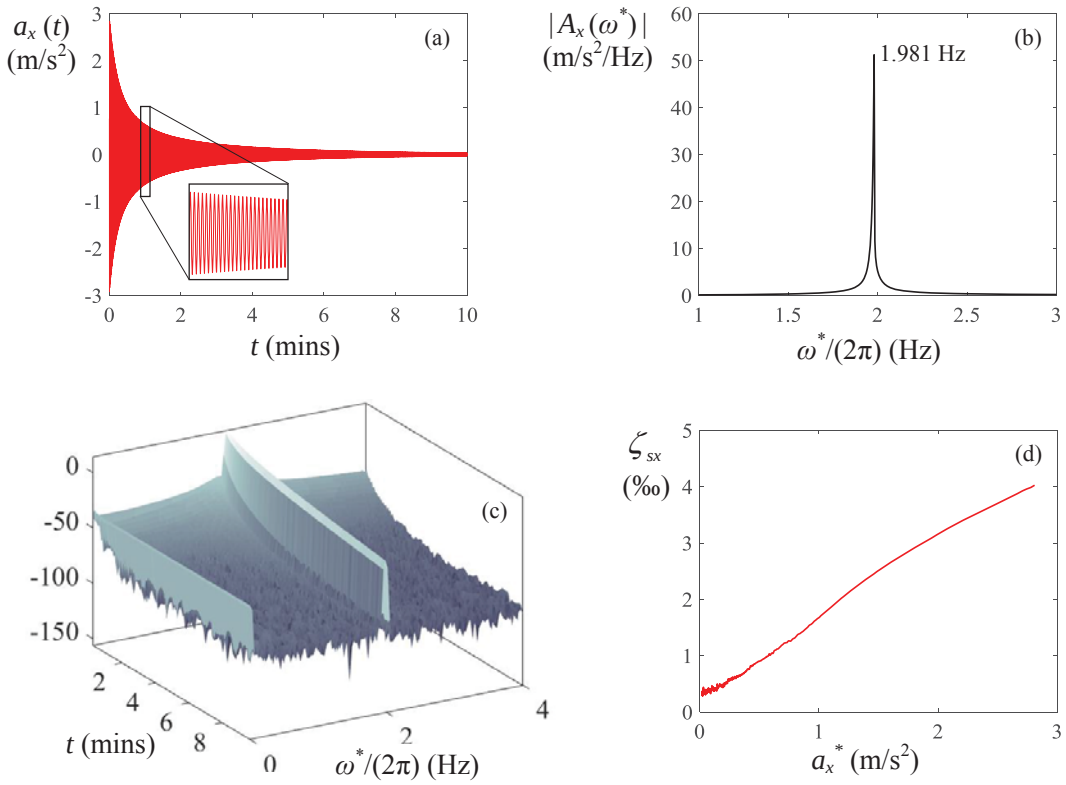
$a_x(t)$ (m/s^2)
(a)
t (mins)
$|A_x(\omega^*)|$ (m/s^2/Hz)
1.981 Hz
(b)
$\omega^*/(2\pi)$ (Hz)
(c)
t (mins)
$\omega^*/(2\pi)$ (Hz)
ζ_{sx} (‰)
(d)
$a_x{}^*$ (m/s^2)

Fig. 9.

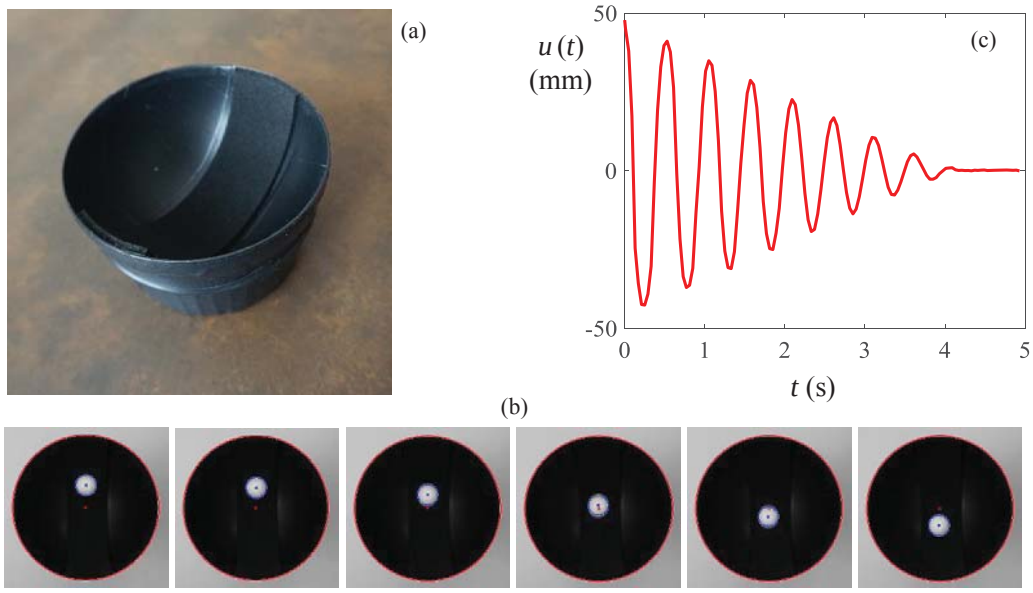

Fig. 10.

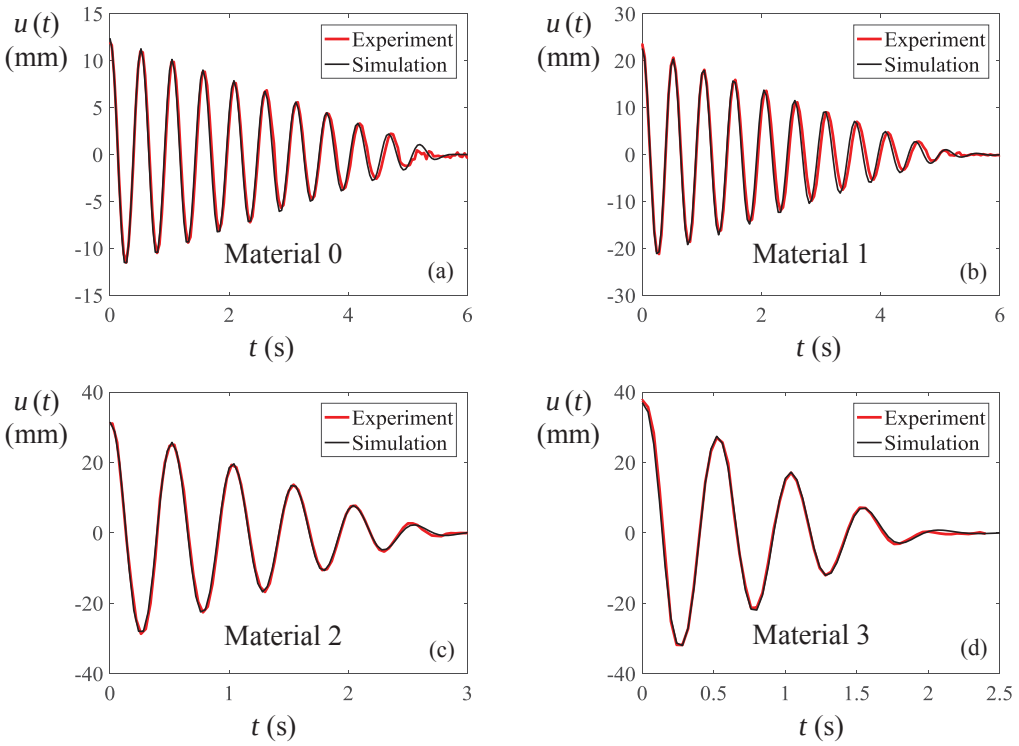
u (t)
(mm)
Experiment
Simulation
Material 0
(a)
t (s)
Material 1
(b)
Material 2
(c)
Material 3
(d)

Fig. 11.

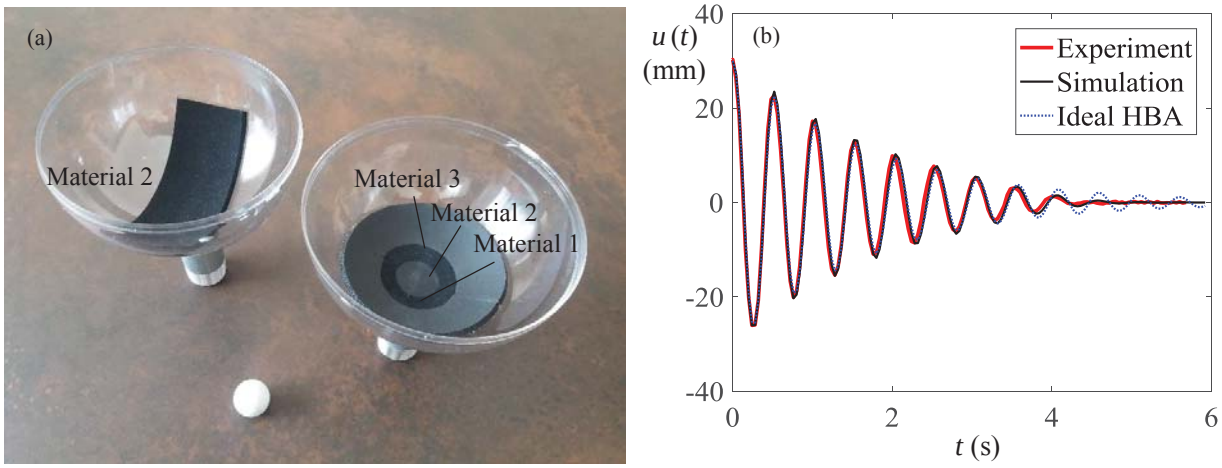
(a)
Material 2
Material 3
Material 2
Material 1
(b)
$u(t)$ (mm)
40
20
0
-20
-40
0
2
4
6
t (s)
Experiment
Simulation
Ideal HBA

Fig. 12.

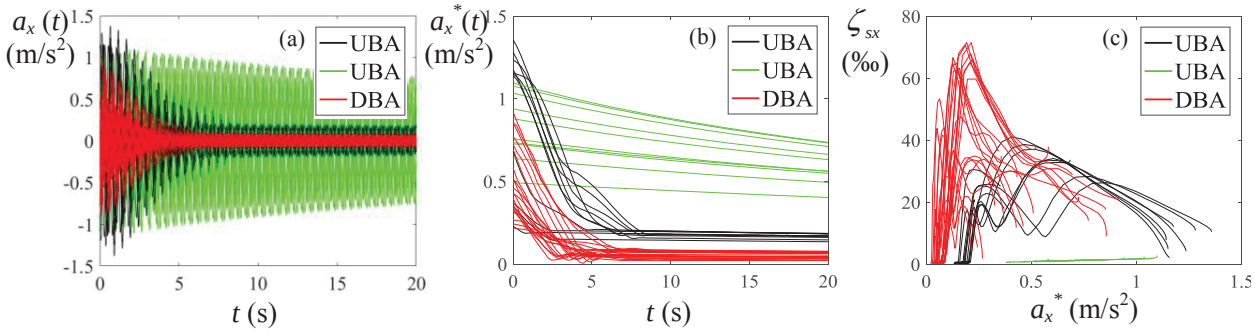
a_x (t) (m/s^2)
(a)
UBA
UBA
DBA
t (s)
a_x^* (t) (m/s^2)
(b)
UBA
UBA
DBA
t (s)
ζ_{sx} (‰)
(c)
UBA
UBA
DBA
a_x^* (m/s^2)

Fig. 13.

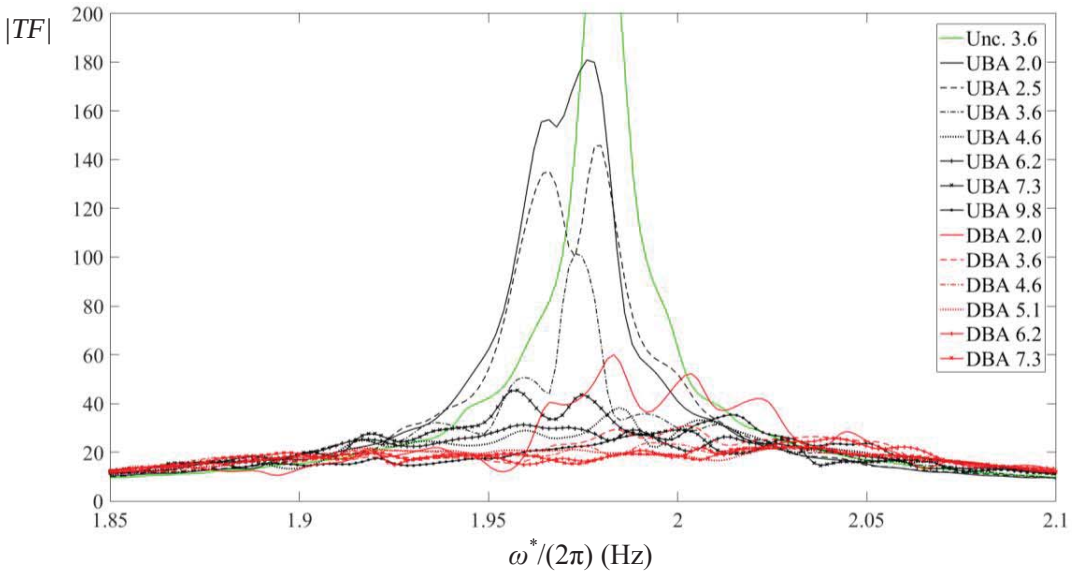
|TF|
200
180
160
140
120
100
80
60
40
20
0
1.85
1.9
1.95
2
2.05
2.1
ω*/(2π) (Hz)
Unc. 3.6
UBA 2.0
UBA 2.5
UBA 3.6
UBA 4.6
UBA 6.2
UBA 7.3
UBA 9.8
DBA 2.0
DBA 3.6
DBA 4.6
DBA 5.1
DBA 6.2
DBA 7.3

Fig. 14.

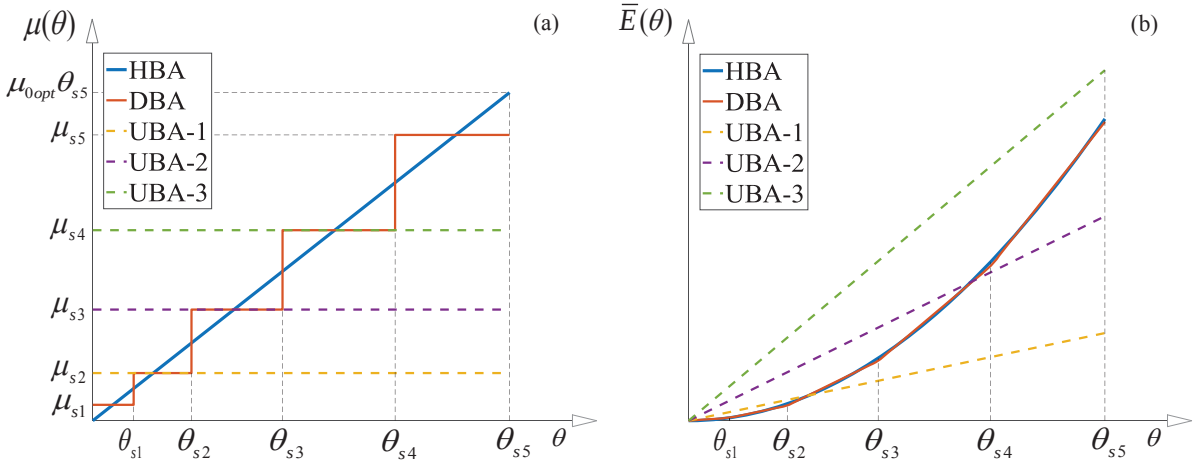
$\mu(\theta)$
(a)
HBA
DBA
UBA-1
UBA-2
UBA-3
$\mu_{0opt}\theta_{s5}$
μ_{s5}
μ_{s4}
μ_{s3}
μ_{s2}
μ_{s1}
θ_{s1}
θ_{s2}
θ_{s3}
θ_{s4}
θ_{s5}
θ
$\bar{E}(\theta)$
(b)
HBA
DBA
UBA-1
UBA-2
UBA-3
θ_{s1}
θ_{s2}
θ_{s3}
θ_{s4}
θ_{s5}
θ

Fig. 15.

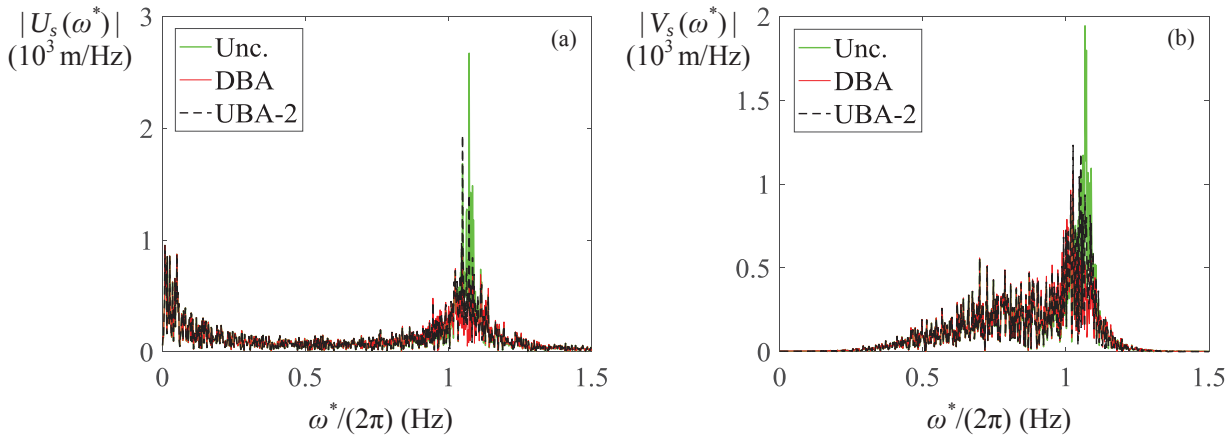
$|U_s(\omega^*)|$
(10^3 m/Hz)
Unc.
DBA
UBA-2
(a)
$\omega^*/(2\pi)$ (Hz)
$|V_s(\omega^*)|$
(10^3 m/Hz)
Unc.
DBA
UBA-2
(b)
$\omega^*/(2\pi)$ (Hz)

Fig. 16.

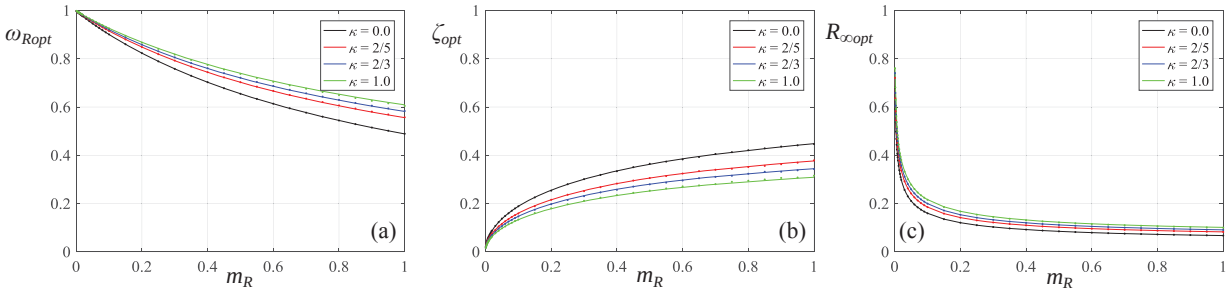
ω_{Ropt}
ζ_{opt}
$R_{\infty opt}$
m_R
$\kappa = 0.0$
$\kappa = 2/5$
$\kappa = 2/3$
$\kappa = 1.0$
(a)
(b)
(c)

Fig. A.1.

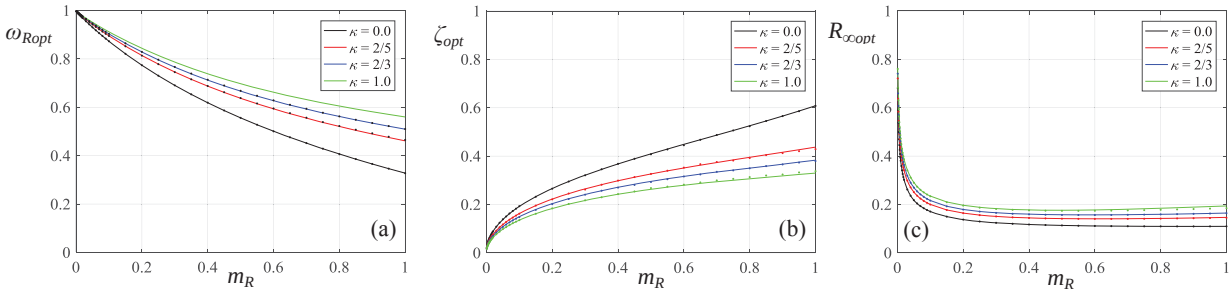
ω_{Ropt}
ζ_{opt}
$R_{\infty opt}$
m_R
$\kappa = 0.0$
$\kappa = 2/5$
$\kappa = 2/3$
$\kappa = 1.0$
(a)
(b)
(c)

Fig. A.2.